A series of [Co(Mabiq)Cl_{2-n}] (n = 0, 1, 2) compounds and evidence for the elusive bimetallic form.

Emma V. Puttock,[‡] *Priyabrata Banerjee,*[§,¶] *Manuel Kaspar,*[†] *Liam Drennen,*[‡] *Dmitry S. Yufit,*[‡] *Eckhard Bill,*[§] *Stephen Sproules,*[‖] *Corinna R. Hess**[,†]

[†]Department of Chemistry and Catalysis Research Center, Technische Universität München, Lichtenbergstrasse 4, D-85747 Garching, Germany

[‡]Department of Chemistry, Durham University, South Rd, Durham, DH1 3LE, United Kingdom

[§]P d{-Sodqfn-

ABSTRACT

The synthesis and characterization of a series of cobalt compounds, coordinated by the redox active macrocyclic biquinazoline ligand, Mabiq (2-4:6-8-bis(3,3,4,4-tetramethyldihydropyrrolo)-10-15-(2,22biquinazolino)-[15]-1,3,5,8,10,14-hexaene-1,3,7,9,11,14-N_6), is presented. The series includes the monometallic Co(Mabiq)Cl_2 ( ), Co(Mabiq)Cl ( ), and Co(Mabiq) ( ), with formal metal oxidation states of +3 ’ +1. A binuclear cobaltous compound, Co_2(Mabiq)Cl_3 ( ), also was obtained, providing the first evidence for the ability of the Mabiq ligand to coordinate two metal ions. The electronic structures of the paramagnetic and were examined by EPR spectroscopy and magnetic susceptibility studies. The Co^{II} ion that resides in the N_4-macrocylic cavity of and adopts a low spin $S = {}^1/_2$ configuration. The bypirimidine functionality in additionally coordinates a high-spin, $S = {}^3/_2$ cobaltous ion in a tetrahedral environment. The two metal ions in are weakly coupled by magnetometry. The square planar, low-valent offers one of a limited number of examples of structurally characterized N_4-macrocyclic Co^{I} compounds. Spectroscopic and DFT computational data suggest that a Co^{II}(Mabiq$^{\bullet}$) description may be a reasonable alternative to the Co^{I} formalism for this compound.

Macrocyclic cobalt complexes have recently become a target of acute focus in the quest for economical and robust solar fuel catalysts.[1-5] Members of this family of compounds, which includes cobalt porphyrins, cobalamins, and cobaloximes, evolve hydrogen electrocatalytically, often operating at modest overpotentials.[6,7] Notably, recent studies have evidenced photocatalytic H_2 production by such systems,[8-11] a vital feature for their integration in an artificial photosystem. [1,12,13]

In-depth mechanistic studies have provided valuable insight into the reactivity of cobalt N_4-macrocyclic complexes and enabled the identification of key reactive intermediates.[1-3,12,14-17] The low-valent Co^I form is commonly the active species in the reaction of the compounds. Protonation of the Co^I species yields a Co^{III}-hydride, from which H_2 is subsequently released via either a homolytic or heterolytic pathway, restoring the cobaltous form of the complexes. The macrocyclic ligands must, therefore, minimally be able to support metal oxidation states ranging from +1 to +3 throughout the catalytic cycle. Co^0 species also have been invoked for hydrogen evolution by cobalt-porphyrins and cobaloximes with weak acids.[1,5,17]

Given the aforementioned series of electron transfer events, the redox activities of the various N_4-macrocyclic ligands are noteworthy. The pyrrole based porphyrin and corrole ligands are readily oxidized.[18,19] Indeed, Spiro et al. anticipated that the porphyrin À-À* transitions could be exploited for formation of a Co^I porphyrin radical cation, offering a route to photochemical hydrogen production.[18] More recently, partial reduction and protonation of the macrocyclic ligand have been proposed to occur in the mechanism of hydrogen evolution by hangman porpyhrins.[20] The diimine moieties of the cobaloximes also are readily reduced.[21,22] Ligand-centered redox processes were established in the chemistry of iron tetraimine complexes,[23] and

by analogy, a Co^{I} cobaloxime ligand radical was proposed as an alternate formulation of the Co^{0} species noted above.[1]

Besides their capacity for hydrogen production, macrocyclic cobalt complexes have proven to be effective catalysts for a variety of other valuable chemical transformations that include cyclopropanation, furanylation, C-H amination, and aziridination reactions.[24-28] The chemistry appears to involve carbene or nitrene transfer from a cobalt(III) porphyrin intermediate. The electronic and steric nature of the porphyrin ligand has a significant influence on the selectivity of these reactions.[25,29] The aforementioned catalytic applications thus further merit the development of new macrocyclic cobalt compounds.

We herein describe the synthesis and characterization of an electron transfer series of cobalt compounds coordinated by the redox-active macrocyclic biquinazoline ligand, Mabiq[30] (Scheme 1). The synthesis and electronic structure studies of zinc- and iron-containing Mabiq complexes were reported previously.[31] These prior studies established the redox-activity of the macrocycle, which is capable of accepting one electron via À*-orbitals of the diketiminate unit. In fact, experimental and computational data illustrated that the low valent, *formally* Fe^{I} compound, Fe(Mabiq), was in actuality an intermediate spin Fe^{II} compound, in which the iron ion is antiferromagnetically coupled to a Mabiq-centered radical.[31]

In light of findings from studies with the iron-containing complexes, we were eager to explore the coordination chemistry of Mabiq with cobalt. Electrochemical studies, detailed in this work, reveal that the Mabiq ligand supports formal cobalt valencies of 0 ’ +3. We have successfully isolated the monometallic Co^{I}, Co^{II} and Co^{III} forms in this redox series. In addition, we have isolated for the first time a bimetallic Mabiq compound, Co_2(Mabiq)Cl_3. The latter compound attests to the ability of the macrocyclic biquinazoline ligand to coordinate a second metal ion.

The results of electronic structure studies on the series of macrocyclic cobalt compounds are presented. The work represents the first chapter in ongoing studies concerning the properties and reactivity of Co-Mabiq compounds.

$CoCl_2$ and $CoCl_2 \cdot 6H_2O$ were purchased from Strem Chemicals, phosphorus pentachloride and phosphorus oxychloride were purchased from Alfa Aesar and DMF was purchased from AGTC Bioproducts. All other reagents were purchased from Sigma Aldrich and used as received, except tetrabutylammonium hexafluorophosphate, which was recrystallized multiple times using ethanol. Metal compounds were synthesized in an inert atmosphere, under nitrogen, using anhydrous solvents. Solvents were dried by passage over activated alumina columns and stored over activated 3 Å or 4 Å molecular sieves. CH_2Cl_2 was dried over phosphorus pentoxide and distilled under Ar prior to use.

H(Mabiq) was synthesized as previously described,[30,31] with the following modification; 4,42-dihydroxy-2,22-biquinazoline was synthesized by heating oxalylbis(anthranilamide) in a round bottom flask, under vacuum, at ~350 °C, using a heating mantle. The resultant dark brown solid was recrystallized from DMF (61% yield) and the product was confirmed by comparison of the IR to previously reported data.[30]

$CoCl_2 \cdot 6H_2O$ (66 mg, 0.28 mmol) was added to an aerated solution of H(Mabiq) (100 mg, 0.18 mmol) and triethylamine (24 µL, 0.19 mmol) in CH_2Cl_2 (10 mL). The solution was left to stir overnight, filtered through Celite and the solvent removed in vacuo, leaving a dark brown solid. The product was recrystallized by slow evaporation of a solution of in CH_2Cl_2 (97 mg, 0.14 mmol, 78% yield).

Anal. Calcd for $C_{34}H_{35}Cl_4CoN_8$: C, 53.99; H, 4.66; N, 14.81. Found: C, 53.85; H, 4.71; N, 14.74. ^{1}H NMR (400 MHz, $CDCl_3$): ´ = 9.19 (dd, *J* = 8.3, 0.8 Hz, 2H), 8.53 (d, *J* = 8.3 Hz, 2H), 8.10 (ddd, *J* = 8.5, 7.0, 1.5 Hz, 2H), 7.89 (ddd, *J* = 8.2, 7.0, 1.1 Hz, 2H), 6.49 (s, 1H), 1.51 (s, 12H), 1.48 (s, 12H). ^{13}C NMR (101 MHz, $CDCl_3$): ´ = 186.8, 177.9, 159.3, 156.7, 151.05, 135.7, 129.5, 129.2, 126.5, 124.2, 94.06, 51.9, 51.7, 24.3, 23.4. ASAP-MS(+) (*m*/*z*): 670 $[M]^+$, 635 [M-

Cl]$^+$, 600 [M-2Cl]$^+$. UV-Vis »$_{max}$ (nm (µ, M^{-1} cm^{-1})) in CH_2Cl_2: 273 (8.0 × 10^4), 322 (3.5 × 10^4), 381 (2.3 × 10^4), 432 (8.0 × 10^3), 484 (1.2 × 10^4), 514 (2.7 × 10^4). IR (cm^{-1}): 2978 w, 2930 w, 1603 m, 1572 m, 1561 m, 1510 s, 1488 m (sh), 1463 s, 1409 m, 1364 s, 1322 w, 1302 w, 1268 m, 1257 w (sh), 1232 m, 1199 w (sh), 1190 w, 1166 s, 1125 m, 1092 s, 1065 s, 1032 m (sh), 1000 m (sh), 963 m, 910 w, 893 m, 878 w, 866 w, 826 m, 813 w, 778 s, 758 m, 737 m (sh), 728 s, 718 m (sh), 697 m, 687 s, 663 w, 638 w, 628 m, 610 s.

$CoCl_2$ (24 mg, 0.18 mmol) was added to a solution of H(Mabiq) (100 mg, 0.18 mmol) and triethylamine (24 µL, 0.19 mmol) in CH_2Cl_2 (10 mL). The solution was stirred overnight, the resultant green solution was filtered through celite and the solvent removed in vacuo, leaving a dark green solid (107 mg, 94.4% yield). Single crystals were obtained by slow evaporation of a concentrated solution of in CH_2Cl_2.

Anal. Calcd for $C_{33}H_{33}CoClN_8$: C, 62.31; H, 5.23; N, 17.62. Found: C, 62.19; H, 5.39; N, 17.52. ASAP-MS(+) (*m*/*z*): 601 [M-Cl]$^+$, 543 [M-CoCl]$^+$. UV-Vis »$_{max}$ (nm (µ, M^{-1} cm^{-1})) in MeOH: 253 (2.9 × 10^4), 271 (2.2 × 10^4), 318 (1.9 × 10^4), 348 (1.7 × 10^4), 427 (7.0 × 10^3), 442 (7.2 × 10^3), 480 (3.6 × 10^3), 576 (2.1 × 10^3), 618 (2.2 × 10^3), 668 (1.7 × 10^3). IR (cm^{-1}): 2973 w, 1597 m, 1571 s, 1558 m (sh), 1544 w (sh), 1509 s, 1484 m, 1461 s, 1412 m, 1365 m, 1339 w, 1324 w, 1302 w, 1296 w (sh), 1270 m, 1255 w, 1242 m, 1195 w, 1167 m, 1123 s, 1097 vs, 1078 vs, 1031 w, 1017 w, 1006 w, 966 w, 958 w, 893 w, 866 w, 813 w, 811 w, 780 s, 763 m, 736 m, 719 w (sh), 702 w (sh), 668 m, 675 w, 663 w, 646 w, 634 w, 630 w, 611 m.

$CoCl_2$ (103 mg, 0.79 mmol) was added to a solution of HMabiq (200 mg, 0.37 mmol) and triethylamine (48 µL, 0.38 mmol) in THF (10 mL). The mixture was stirred overnight, and the resultant green precipitate was filtered and washed with THF (3 × 1 mL) and CH_2Cl_2 (3 × 1 mL) to give the dark green solid (269 mg, 95% yield).

Anal. Calcd for $C_{33}H_{33}Co_2Cl_3N_8$: C, 51.75; H, 4.34; N, 14.63. Found: C, 51.75; H, 4.28 N, 14.48. ASAP-MS(+) (*m*/*z*): 601 $[M\text{-}CoCl_3]^+$. UV-Vis »$_{max}$ (nm (µ, M^{-1} cm^{-1})) in MeOH: 253 (5.1 × 10^4), 271 (4.2 × 10^4), 318 (3.7 × 10^4), 348 (3.0 × 10^4), 427 (1.5 × 10^4), 442 (1.6 × 10^4), 480 (7.4 × 10^3), 576 (4.5 × 10^3), 618 (4.6 × 10^3), 668 (3.5 × 10^3). IR (cm^{-1}): 2967 w, 1560 s, 1502 m, 1488 m, 1474 s (sh), 1460 s, 1431 m (sh), 1409 s, 1378 m, 1362 m, 1306 w, 1276 w, 1257 w, 1228 m, 1200 w, 1169 m, 1125 m, 1094 s, 1072 s, 974 w, 956 w, 897 m.

Cp_2Co (12.7 mg, 0.067 mmol) was added to a suspension of (42.7 mg, 0.067 mmol) in THF (5 mL), upon which the mixture immediately turned a deep purple. The reaction was stirred for 2 h, filtered through Celite and the solvent removed in vacuo, yielding a purple solid (35 mg, 87% yield). Single crystals were obtained by slow evaporation of a concentrated solution of in THF or alternatively, by slow diffusion of pentane into a solution of in THF.

Anal. Calcd for $C_{33}H_{33}CoN_8$: C, 65.99; H, 5.54; N, 18.66. Found: C, 66.16; H, 5.62; N, 18.34. ^{1}H NMR (400 MHz, THF-d_8): ´ = 9.06 (dd, *J* = 8.2, 0.9 Hz, 2H), 8.37 (d, *J* = 8.1 Hz, 2H), 8.19 (td, *J* = 7.6, 2H), 7.64 (td, *J* = 7.6, 2H), 7.54 (s, 1H), 1.55 (s, 12H), 1.39 (s, 12H). ASAP-MS(+) (*m*/*z*): 600 $[M]^+$. UV-Vis »$_{max}$ (nm (µ, M^{-1} cm^{-1})) in THF: 268 (4.4 × 10^4), 324 (3.5 × 10^4), 335 (3.7 × 10^4), 392 (1.9 × 10^4), 403 (2.4 × 10^4), 523 (1.3 × 10^4), 533 (1.4 × 10^4), 913 (2.8 × 10^3), 1048 (2.0 × 10^3), 1210 (2.1 × 10^3). IR (cm^{-1}): 2971 w, 2906 w, 1608 w, 1591 w (sh), 1564 m, 1548 m, 1506 m, 1480 m, 1463 w, 1446 m, 1414 m, 1388 w, 1374 m, 1364 m (sh), 1354 m, 1325 w, 1280 m, 1253 w, 1222 m, 1187 vw, 1164 m, 1149 m, 1136 s, 1109 m (sh), 1016 w, 967 w, 954 vw, 896 w, 867 m, 819 w (sh), 813 m, 792 vw, 765 vs, 748 s, 696 m, 690 m, 673 m, 632 m, 625 m, 612 m.

NMR spectra were recorded on a Bruker Avance-400 (400 MHz ^{1}H, 100 ^{13}C MHz) spectrometer. Electronic spectra were recorded on a Perkin-Elmer Lambda 900

spectrophotometer. Diffuse reflectance spectra were obtained by fixed-angle oblique illumination of the sample using an Energetiq LDLS EQ-99 broadband lamp and collection perpendicular to the face of the sample using an Ocean Optics Maya Pro 2000 spectrometer. Data were recorded using the Ocean Optics software, and integration times were adjusted to afford maximum response of the spectrometer without saturation of the detector. NaCl was used as the white standard. Mass spectra were measured using a LCT Premier XE mass spectrometer and an Acquity UPLC (Waters Ltd, UK). Infrared spectra were recorded using a Perkin Elmer Spectrum 100 spectrometer. Microanalyses were performed at the London Metropolitan University or at the microanalytical laboratory of the Technische Universität München. Electrochemical measurements were carried out using a Palm Emstat2 potentiostat using a three electrode cell equipped with a Pt auxiliary electrode, a glassy carbon working electrode and either a $Ag/AgNO_3$ or Pt electrode (CH_2Cl_2) as the reference. Potentials are reported with reference to an internal standard ferrocenium/ferrocene ($Fc^{+/0}$). Magnetic susceptibility data (2-290 K) were recorded using a SQUID magnetometer (MPMS7, Quantum Design) in a 1 T external field. Data were corrected for underlying diamagnetism using tabulated Pascal's constant and fit using julX (Dr. E. Bill). EPR measurements were carried out at the EPSRC National UK EPR Facility and Service in the Photon Science Institute at The University of Manchester. X-band spectra were collected on a Bruker EMX Micro spectrometer and simulations performed using Bruker's Xsophe software package.[32]

X-ray single crystal data for and were collected at 120.0(1) K on a Bruker D8Venture diffractometer (PHOTON-100 CMOS detector, IμS-microsource, focusing mirrors, »MoK±, » = 0.71073Å) and on a Rigaku Saturn 724+ diffractometer (compound) at station I19 of the

Diamond Light Source synchrotron (undulator, λ = 0.6889 Å, ω-scan, 1.0°/frame) and processed using Bruker APEXII software. The temperature of the samples was maintained by the Cryostream (Oxford Cryosystems) open-flow nitrogen cryostats. All structures were solved by direct method and refined by full-matrix least squares on F^2 for all data using Olex2[33] and SHELXTL[34] software. All non-disordered non-hydrogen atoms were refined anisotropically, hydrogen atoms in structures and were refined isotropically, hydrogen atoms in the structure were placed in the calculated positions and refined in riding mode.

All DFT calculations were performed with the ORCA program package.[35] The geometry optimizations of the complexes were performed at the B3LYP level of DFT.[36-38] The all-electron Gaussian basis sets were those developed by the Ahlrichs group.[39,40] Triple-¶ quality basis sets TZV(P) with one set of polarization functions were used on the metals and on the atoms directly coordinated to the metal centre.[41] For the carbon and hydrogen atoms, slightly smaller polarized split-valence SV(P) basis sets were used, that were of double-¶ quality in the valence region and contained a polarizing set of d-functions on the non-hydrogen atoms.[42] Auxiliary basis sets used to expand the electron density in the resolution-of-the-identity (RI) approach were chosen, where applicable, to match the orbital basis.[43,44] The SCF calculations were tightly converged (1×10^{-8} E_h in energy, 1×10^{-7} E_h in the density change, and 1×10^{-7} in maximum element of the DIIS error vector). The geometry optimizations for all complexes were carried out in redundant internal coordinates without imposing symmetry constraints. In all cases the geometries were considered converged after the energy change was less than 5×10^{-6} E_h, the gradient norm and maximum gradient element were smaller than 1×10^{-4} E_h $Bohr^{-1}$ and 3×10^{-4} E_h $Bohr^{-1}$, respectively, and the root-mean square and maximum displacements of all atoms were smaller than 2×10^{-3} Bohr and 4×10^{-3} Bohr, respectively. Single point-calculations on the non-

optimized structures, using the coordinates obtained crystallographically, also were carried out using the B3LYP functional. The results of unrestricted (UKS) calculations were compared to those obtained using the broken-symmetry (BS)[45-47] approach, for calculations on both the optimized and non-optimized geometries. Corresponding and canonical orbitals[48] and density plots were created using GaussView.[49]

The Co^{III} and Co^{II}-Mabiq complexes were synthesized in straightforward reactions of the macrocyclic ligand with $CoCl_2$ starting materials (Scheme 2). For the synthesis of $Co^{III}(Mabiq)Cl_2$ ( ), we initially followed a protocol similar to that employed for the synthesis of $Co(Mabiq)CN_2$,[30] using $CoCl_2 \cdot 6H_2O$ as the source of metal ion, and H_2O_2 as an oxidant. However, higher product yields were obtained by simply allowing HMabiq and $CoCl_2 \cdot 6H_2O$ to react in aerated CH_2Cl_2 solutions, with O_2 as the oxidant. The ^1H NMR spectrum of the diamagnetic shows an upfield shift of the aromatic and diketiminate C-H protons, compared to the spectrum of the free HMabiq ligand (Figure 1), attributable to the presence of the Co^{III} ion in the macrocyclic cavity. The electronic spectrum of (Figure 2), with absorption bands at $»_{max}$ = 484 and 514 nm, resembles that of Zn(Mabiq)Cl ($»_{max}$ = 471 and 502 nm) and $Co(Mabiq)(CN)_2$ ($»_{max}$ = 502 and 536 nm).[30,31] The features in the visible region of the latter complex were ascribed to Mabiq À-À* transitions by von Zelewsky, and the energy deemed dependent on the charge of the coordinated metal ion.[30] The position of these absorption bands among the spectra of , $Zn^{II}(Mabiq)Cl$, $Co^{III}(Mabiq)(CN)_2$ and $Fe^{III}(Mabiq)Cl_2$ ($»_{max}$ = 524 nm) appear to be consistent with this conclusion.

Von Zelewsky's original motivation for the synthesis of the biquinazoline ligand was the design of a bimetallic complex with photocatalytic properties.[30] The Mabiq ligand offers two

potential metal coordination sites, as depicted in Scheme 1. The primary coordination site is furnished by the N_4-cavity, but the external diimine moiety of the bipyrimidine provides an additional metal binding site. The binuclear complexes targeted by von Zelewsky were never subsequently reported. We also were not able to isolate or obtain evidence for the formation of binuclear products in prior studies pertaining to the coordination chemistry of Mabiq with iron. However, we have now generated both mono- and bi-metallic cobaltous complexes, Co(Mabiq)Cl ( ) and Co_2(Mabiq)Cl_3 ( ) upon reaction of HMabiq with either one or two equivalents of anhydrous $CoCl_2$, respectively. Complex offers, for the first time, evidence for the ability to coordinate a metal ion to the secondary Mabiq binding site.

The solid state composition of the bimetallic was verified by elemental analysis. On the basis of elemental analysis, the known structure of , and magnetic susceptibility data for both compounds (vide infra), we propose the structure of as shown in Scheme 2: the coordination environment of the metal ion in the primary Mabiq binding site is akin to that in , while the second cobaltous site is four-coordinate tetrahedral, ligated by two chlorides and the bipyrimidine nitrogens. Minor differences in the visible-NIR region are apparent between the solid-state spectra of and (Figure S3), and the solid-state IR spectra of the two compounds also exhibit several distinctive bands in the fingerprint region (Figure S4). Compounds and have markedly different solubilities in CH_2Cl_2, in which only the monometallic complex is soluble, but both compounds are soluble in CH_3OH. Surprisingly, the solution absorption spectra of and in CH_3OH are superimposable (Figure 2), exhibiting identical transitions in the UV – NIR region (250 – 900 nm), that differ only in the values of their extinction coefficients. The similarity of the spectra suggests that the $CoCl_2$ moiety occupying the outer diimine site of may only be weakly bound, dissociating in solution.

The final compound in this series, the low-valent Co(Mabiq) ( ), was generated upon reduction of with $CoCp_2$ in THF. The ^1H NMR spectrum of the diamagnetic compound in THF-d_8 is shown in Figure 1. A notable feature in the NMR spectrum is the diketiminate C-H proton signal, which appears at 7.54 ppm, significantly upfield in comparison to its position in the spectrum of the diamagnetic Co^{III}-, Fe^{II}-, and Zn^{II}-Mabiq complexes.[31] The solution electronic spectrum of the purple in THF exhibits the common À-À* transitions at $»_{max}$ =392 and 403 nm, as well as absorption bands at $»_{max}$ =523 and 533 nm, which we tentatively assign as MLCT transitions. In addition, multiple features can be seen in the NIR region (750 – 1300 nm, Figure 2). In this respect, the spectrum of closely resembles that of Co^{I}(cobalamin).[50] The absorption spectrum of the superreduced vitamin B_{12} also displays low energy transitions between 500 – 1100 nm, which were assigned as Co 3d ' corrin À* excitations, based on TDDFT computational studies. The relevant vitamin B_{12} À* orbitals are predominantly localized on the diketiminate group of the corrin ring. It is therefore not unreasonable that a similar Co ' Mabiq transition, involving the À* orbitals of the redox-active diketiminate functionality, might account for the NIR transitions in the spectrum of . Though, in depth computational analysis will be required to detangle the various possible contributions to these low energy bands.[51]

The cyclic voltammograms for complexes – are shown in Figure 3. The CVs of and are very similar. In each case an irreversible redox event occurs at $E_{1/2}$ = ~ 0.1 V (vs. $Fc^{+/0}$) that can be assigned to the $Co^{III/II}$ couple. The oxidative process is followed by a reversible one-electron reduction at $E_{1/2}$ = ~ -0.9 V and a second irreversible reductive event at E_a = ~ -1.5 V (Table 2). All three redox events, likewise, are apparent in the CV of (in THF), but are shifted to more negative potentials, and all appear to be reversible.[52] The presence of the axial ligand clearly has a substantial effect on the electrochemical potentials.

Ligand-centered reduction, as established for the Zn- and Fe-Mabiq complexes, occurred at potentials of -0.9 – -1.5 V.[31] The second redox process in the CVs of , and , formally corresponding to the $Co^{II/I}$ couple, thus can be attributed to formation of either a Co^{I}(Mabiq) or a Co^{II}(Mabiq$^{\bullet}$) species. The ensuing redox event, again *formally* described by Co^{0} formation, likely entails formation of $[Co^{I}(Mabiq^{\bullet})]^{1-}$, in which both the metal ion and the ligand are one-electron reduced.

The presence of an additional Co^{II} ion in the bimetallic has a negligible effect on the electrochemistry, compared to the redox behavior of the monometallic compounds. Redox processes apart from those ascribed to the cobalt ion in the macrocyclic cavity are not observed in the range of -1.2 to +0.8 V. The potentials of the $Co^{III/II}$ and $Co^{II/I}$ couples are equivalent to those of and . The $Co^{I/0}$ couple is indiscernible though, and scanning at potentials more negative than -1.2 V led to the appearance of new redox waves (Figure S5). The discrepancies in the redox behavior of and intimate different chemical compositions for the two cobaltous products in solution. Nevertheless, the lack of any redox couples obviously associated with the (bipyrimidine)$CoCl_2$ moiety is surprising. Redox deactivation by a neighboring metal ion has been observed previously in bimetallic complexes,[53] and may be operational in our system. However, the presence of any free $CoCl_2$ in solution, stemming from the dissociation of , also would complicate the electrochemistry. As we presently cannot confirm the solution state composition of , we are unable to draw any further conclusions from the CV regarding the influence of the second cobalt site.

Single crystals were obtained for the monometallic complexes, , and , and the solid state structures are shown in Figure 4. The coordination number of the cobalt complexes decreases according to the formal metal valency: complex is 6-coordinate pseudo-

octahedral, complex adopts a five-coordinate square pyramidal geometry, whereas complex is four-coordinate square planar. In all structures, the dihydropyrrole backbone of the macrocycle is arrange in the 'syn' conformation, as previously denoted for metal-Mabiq complexes.[30,31] The bipyrimidine unit of the Mabiq ligand exhibits varying degrees of distortion among the series of compounds. The macrocyclic ligand is severely buckled in , which also results in a ~6° difference in coplanarity between the two pyrimidine groups. The torsion angle of the C–C bond joining the quinazoline unit is significantly reduced in (1.8°), and may account in part, for the existence of both mono- and bi-nuclear forms of the cobaltous complex.

The Co–N distances among the three monometallic complexes reflect the typical asymmetric metal coordination,[30,31] with slightly shorter bonds to the diketiminate nitrogen atoms, versus to the bipyrimidine unit (Table 3). The average Co–N bond lengths of and are comparable ($Co(Mabiq)Cl_2$: $Co–N_{avg}$ = 1.91 Å; Co(Mabiq)Cl: $Co–N_{avg}$ = 1.90 Å). However, the metal-nitrogen bond distances of are significantly shorter ($Co–N_{avg}$ = 1.87 Å), denotive of significant metal to ligand À-backbonding. The bond lengths of the diketiminate unit of also are noteworthy, considering that this component represents the redox-active functionality of the macrocycle. The average C–C bond distance of this unit is slightly shorter than the analogous bond length in and , whereas the C–N bonds are considerably longer. Similar bond distances were observed in the reduced $Fe^{II}(Mabiq^{\bullet})$ complex.[31] The structural data further highlights the issue regarding the most accurate description of the low valent Co(Mabiq) compound: whether $Co^{I}(Mabiq)$ or $Co^{II}(Mabiq^{\bullet})$.

The electronic structures of the paramagnetic mono- and bi-metallic Co^{II} complexes, and , were examined using EPR spectroscopy and SQUID magnetometry. Magnetic susceptibility data for (2 – 300 K, 1 T; Figure S6) afford a temperature independent

μ_{eff} = 1.88 μ_B, and g = 2.17, establishing an $S = {}^1/_2$ ground state for the Co^{II} complex. The X-band EPR spectrum recorded in CH_2Cl_2/toluene solution at ambient temperature is indicative of a low-spin Co^{II} center (Figure S7). Coupling to the ^{59}Co ($I = {}^7/_2$, 100% natural abundance) nucleus produces an 8-line hyperfine splitting of the electron spin resonance. Successful simulation was achieved using g_{iso} = 2.204 and A_{iso} = 55 × 10^{-4} cm^{-1}, and a Kivelson lineshape model that accounts for the uneven profile of the hyperfine lines brought about by motional tumbling of in the solvent mixture.

At 30 K, the frozen solution spectrum is richly detailed with hyperfine structure (Figure 5). Simulation was achieved using g = (2.280, 2.280, 2.002) and $A\{^{59}Co\}$ = (35, 36, 111) × 10^{-4} cm^{-1}. The axial splitting of the principal g- and A-values, where $g_\perp > g_\parallel \sim g_e$ and $A_\perp < A_\parallel$ are diagnostic of a ^2A ground term of a Co^{II} ion with a $(d_{xy,xz,yz})^6(d_{z^2})^1$ electron configuration. The magnitude of the g-anisotropy is indicative of a five-coordinate low-spin Co^{II} ion, and markedly different to a four-coordinate species.[54,55] Interestingly, the axially split spectrum is more akin to Co^{II} ions encapsulated by symmetric macrocycles such as porphyrins and phthalocyanines.[56-62] Removal of in-plane symmetry provided by corrins,[63,64] corroles,[65-68] and Schiff base macrocycles,[69,70] introduces significant rhombicity in the g-values ($g_x > g_y$), which is seemingly negated by the diketiminate unit in Mabiq. The presence of a single apical Cl^- ligand manifests in the additional hyperfine splitting of the parallel hyperfine lines to high field. Six of these features are visible with the missing two overlapping with the perpendicular components to lower field. This structure was accommodated in the simulation with a coupling to the $^{35,37}Cl$ ($I = {}^3/_2$) nucleus of 25 × 10^{-4} cm^{-1}. Only the parallel contribution (A_z) is resolved in the spectrum which has been observed for numerous Lewis base adducts of Co^{II} ions in an N_4 macrocycle.[63,68,71,72]

Magnetic susceptibility measurements for the dicobalt complex, , show a temperature independent magnetic moment from 50 – 300 K, yielding a value of μ_{eff} = 4.3 μ_B, which decreases below 50 K to a value of μ_{eff} ~ 3.2 μ_B (Figure 6). The room temperature value of the magnetic moment is fully consistent with the presence of two Co^{II} ions , with $S = {}^1/_2$ and $S = {}^3/_2$ ground states (the spin only value for two uncoupled $S = {}^1/_2$ and $S = {}^3/_2$ ions is μ_{eff} = 4.24 μ_B, for g = 2). The data were fit according to the following spin-Hamiltonian:

$$\hat{—} = -2J\hat{S}_1 \cdot \hat{S}_2 + g\mu_B(\hat{S}_1 + \hat{S}_2) \cdot B + \sum_{i=1,2} D[\hat{S}_z^2 - \tfrac{1}{3}S_i(S_i+1) + \tfrac{E}{D}(\hat{S}_{x,i}^2 - \hat{S}_{y,i}^2)]$$

including exchange coupling (J) and zero-field splitting (ZFS) terms, with $S_1 = {}^1/_2$, $S_2 = {}^3/_2$. The data were best fit with g_1 = 2.05, g_2 = 2.0, J = 0.47 cm^{-1}, $|D_2|$ = 20.37 cm^{-1}. The miniscule exchange coupling constant denotes weak coupling between the two Co^{II} centers. The value of the ZFS for the high-spin Co^{II} ion is consistent with the values observed for tetrahedral cobaltous compounds, which can range widely depending on the ligand field and degree of distortion from tetrahedral geometry.[73-77] The data fully support the solid state bimetallic assignment of previously surmised: the low-spin ($S = {}^1/_2$) cobaltous ion resides in the macrocylic cavity, additionally ligated by an axial chloride ligand, whereas the second cobaltous site adopts the expected high-spin, $S = {}^3/_2$, configuration expected for a d^7 ion in a tetrahedral environment.

The fluid solution EPR spectrum of in methanol is essentially identical to that for (Figure S8) with g_{iso} = 2.196 and A_{iso} = 49 × 10^{-4} cm^{-1}. The overall profile is slightly more askew than for which is a consequence of the increased mass of the molecule or simply a change of solvent. The hyperfine pattern reveals the observable resonances can arise from a unique single spin only, presumably the square pyramidal $S = {}^1/_2$ Co^{II} ion, as the electron spin relaxation in the high spin center precludes its appearance in fluid solution. The frozen solution spectrum recorded in CH_3OH/toluene solution at 10 K consists of a broad signal at ~120 mT attributed to

an $S = {}^3/_2$ species and a second signal at ~300 mT consistent with the assumed spin doublet observed at room temperature (Figure S9). This spectrum is additional evidence for the dissociation of bimetallic in solution, as the spectral profile cannot be reproduced using the spin-Hamiltonian parameters obtained from fitting of the magnetic susceptibility data (Figure 6). The high-field signal exhibits six peaks readily ascribed to the $A_{\|}$ of the low-spin Co^{II} center (the remaining two are obscured by the perpendicular components), with a coupling nearly identical to that measured for (vide supra). Notably these peaks lack the superhyperfine splitting to the apical Cl^- ligand, suggesting this has been replaced by either MeOH or water. However, they are too weak to be associated with the bulk of the signal centered at ~300 mT, whose four prominent peaks cannot be readily interpreted at this stage. Dissociation liberates the high-spin Co^{II} ion which presumably generates the broad signal at ~120 mT. This subspectrum has been simulated as an $S = {}^3/_2$ species with $D >> h½$yielding axial g = (2.35, 2.35, 2.58) with a small rhombic contribution to the ZFS of E/D = 0.03 (dashed line, Figure S9). The simulation employed a large Gaussian linewidths, W = (450, 450, 1000) × 10^{-4} cm^{-1}, and E/D strain ($\tilde{A}_{E/D}$ = 0.22). These parameters match those of related tetrahedral Co^{II} compounds.[78]

The ambiguity concerning the oxidation state of the cobalt ion in prompted us to carry out density functional theory (DFT) investigations (B3LYP) of the low valent compound. Calculations were carried out using either the spin-unrestricted (UKS) or broken symmetry (BS) approach on the geometry optimized structure. The experimentally derived and geometry optimized structures differed slightly with respect to the extent of distortion of the macrocyclic ligand (Table 3 and S1 – S3). Therefore, the results were further compared to single point energy calculations performed on the non-optimized, crystallographically determined structure of , to examine whether minor geometric perturbations would bias the electronic structure. The relevant

DFT-derived, metal-based MOs from calculations on either structure were nearly identical in character, though variations in their relative energies were occasionally observed (Figures 8 and S10). A lower energy solution was consistently provided by the BS approach (~ 2.4 kcal mol^{-1}) versus the UKS calculation, which converged to a closed-shell solution.

The BS calculations describe a $Co^{II}(Mabiq^{\bullet})$ electronic structure for . The DFT derived spin density map (Figure 7) depicts one unpaired spin on the cobalt center, and one unpaired spin of opposite sign on the Mabiq ligand. The qualitative MO diagram (Figure 8) depicts a singly occupied metal-based orbital (d_{xz}) of ±-spin that has a spatial overlap of 0.57 with a ligand-centered SOMO, occupied by the electron of ²-spin. Analogous to the findings from computational studies on $Fe^{II}(Mabiq^{\bullet})$ and $Zn^{II}(Mabiq^{\bullet})$, the ligand-centred electron is localized on the diketiminate component of the macrocycle. Nonetheless, the small energy difference between the BS and UKS solutions precludes an unambiguous assignment of the oxidation levels in , whose electronic structure is best represented by the resonance forms $Co^{I}(Mabiq)$ ” $Co^{II}(Mabiq^{\bullet})$.

The coordination chemistry of Mabiq with cobalt is similar to that of its neighbouring transition metal, iron, likewise allowing for isolation of a three-electron series of monometallic compounds (, and). The metal ion in the square pyramidal environment of , adopts a low-spin $S = {}^{1}/_{2}$ configuration, and judging from the EPR data, is a genuine d^7 cobaltous compound. This contrasts with the isoelectronic Fe(Mabiq), in which the macrocyclic ligand is in the reduced $(Mabiq^{\bullet})^{1-}$ form and coordinates an $S = 1$ ferrous ion. Compound is the most interesting amongst the monometallic cobalt compounds. As noted previously, the Co^{I} forms of related macrocyclic complexes have garnered attention due to the activity of these species with

respect to H_2 production. The Co^{I} form of cobaloximes, analogous to vitamin B12, are strong nucleophiles that also readily react with alkylating agents and olefins.

The exact electronic structure of our {Co(Mabiq)} cannot be unambiguously defined owing to the pervasive metal-ligand covalency that precludes assignment of oxidation states.[22,79] Nevertheless, the combined spectroscopic and DFT data for suggest that significant electron density resides on the diketiminate moiety of the N_4-ligand, such that its true electronic structure lies between the Co^{I}(Mabiq) and Co^{II}(Mabiq$^{\bullet}$) limiting forms.

Electrochemistry data illustrate that further reduction of both the Fe(Mabiq) and Co(Mabiq) compounds is possible, yielding the formally 'Fe^{0}' and 'Co^{0}' monoanionic species respectively. Both of these species are likely to comprise the reduced form of the macrocycle. The Mabiq ligand clearly offers an additional electron storage site and the redox properties of this ligand render metal-mabiq compounds promising candidates as catalysts for multi-electron reactions. Access to both the one- and two-electron reduced forms of also presents an opportunity to compare the reactivity of both forms with respect to hydrogen production. These aspects are the focus of ongoing studies in our group.

A surprising result of our studies was the synthesis of the bimetallic . While the functionalities of Mabiq appear well-suited to the coordination of two metal ions, binuclear compounds had thus far been elusive. We conclude, based on the solution state spectroscopic data for the binuclear compound, that the second metal site is only weakly bound and readily ousted from the bipyrimidine by competing ligands (e.g. solvent molecules). Nevertheless, the evidence in support of formation of the dicobalt complex in the solid state, warrants further examination of the factors that contribute to the activation of the second binding site. The

coordination chemistry of other metals at this site, and modifications to enhance the chelating ability of the external unit are additional research avenues that we are currently exploring.

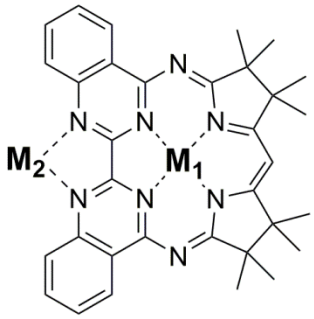
M2
M1
N

Synthesis of compounds – .

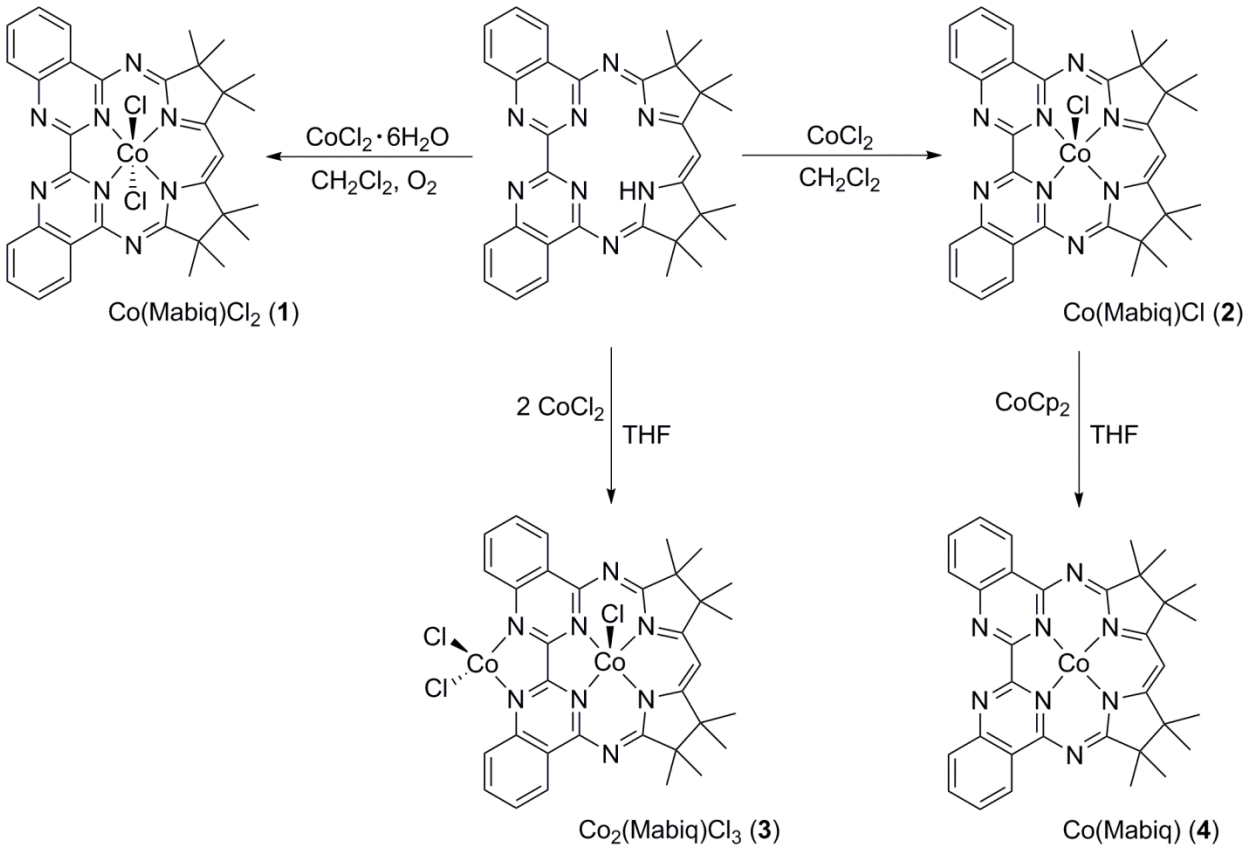

^{1}H NMR spectra of HMabiq (top, $CDCl_3$), (middle, $CDCl_3$), and (bottom, THF-d_8), showing the aromatic protons and diketiminate proton (*) for comparison.

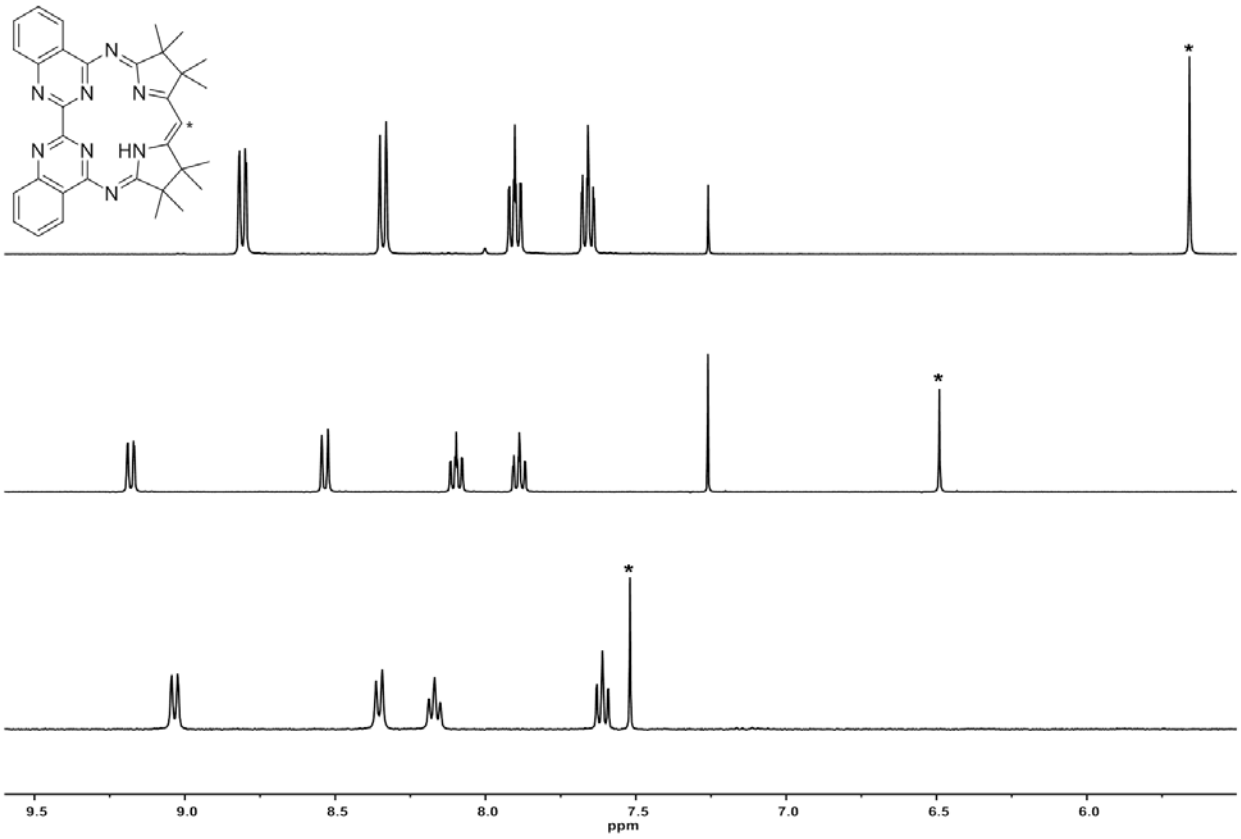

Electronic spectra of (red, CH_2Cl_2), (green, CH_3OH), (blue, CH_3OH) and (purple, THF). Inset: NIR region of spectrum of .

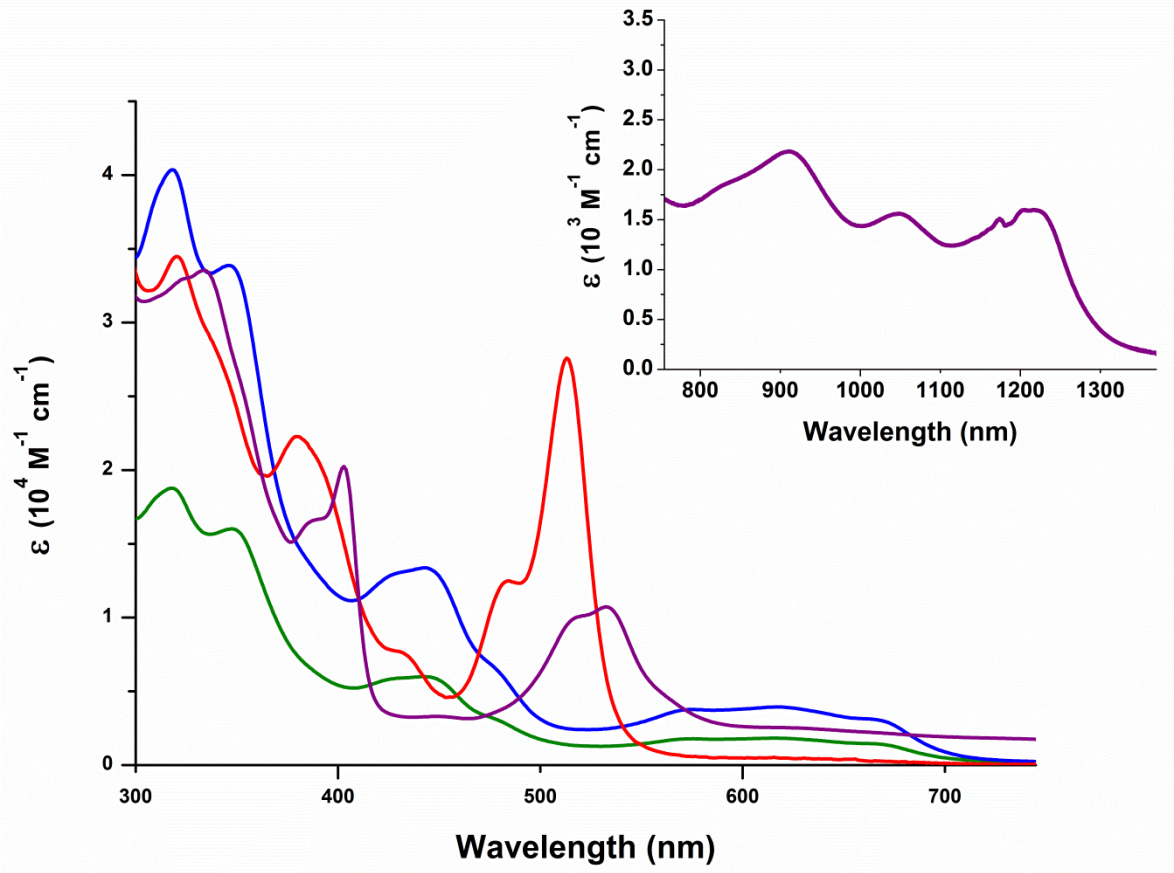

Cyclic voltammograms of – , 0.2 V s^{-1}, 0.1 M $[N(n\text{-}Bu)_4]PF_6$. CV of in THF, all others in CH_3OH.

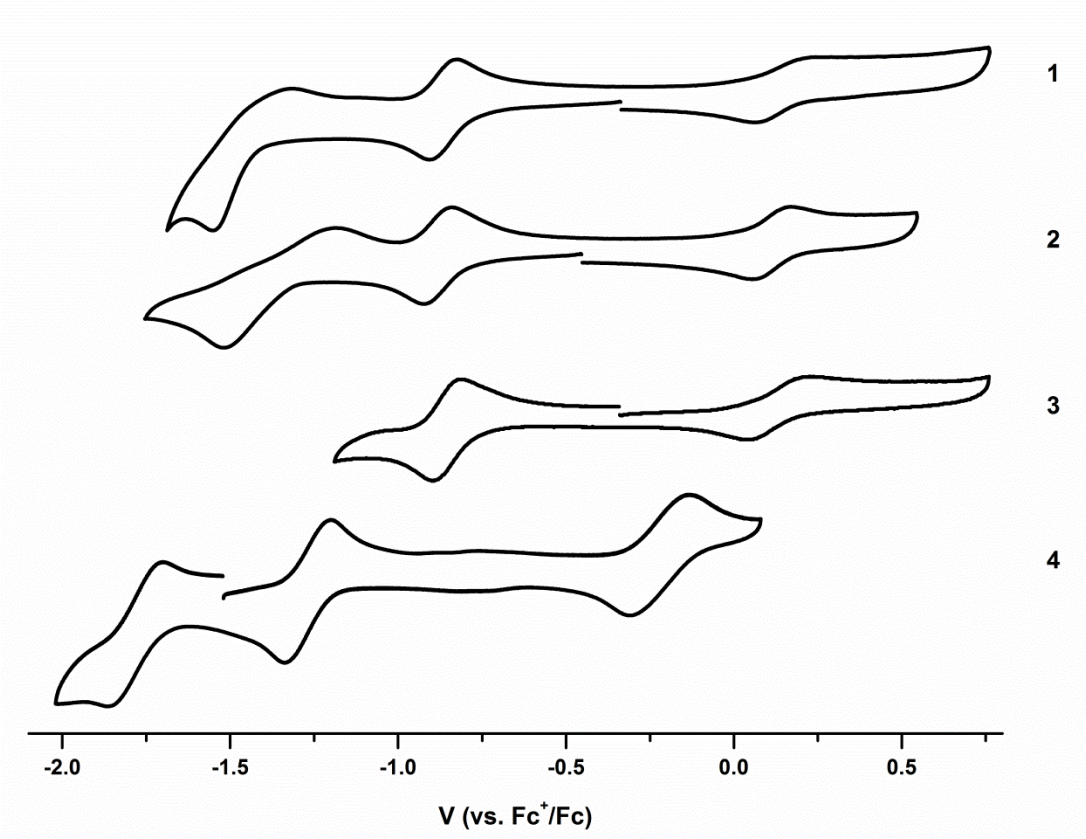

Molecular structures of , and (50% probability ellipsoids). Hydrogen atoms and solvent molecules omitted for clarity.

1

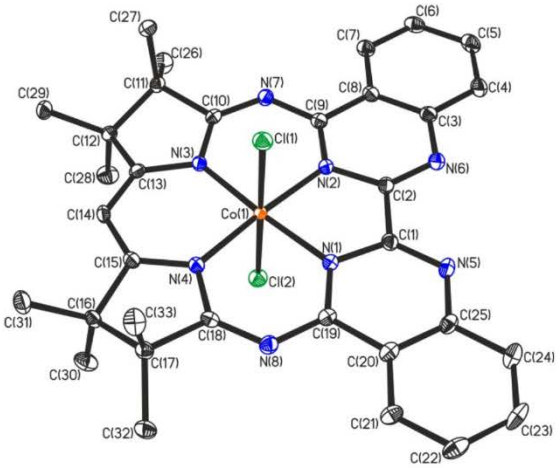

2

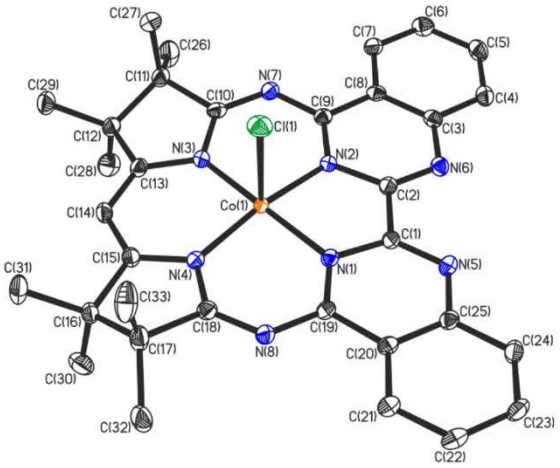

4

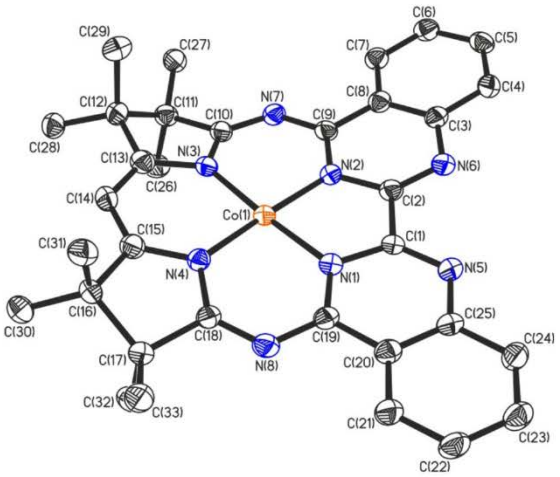

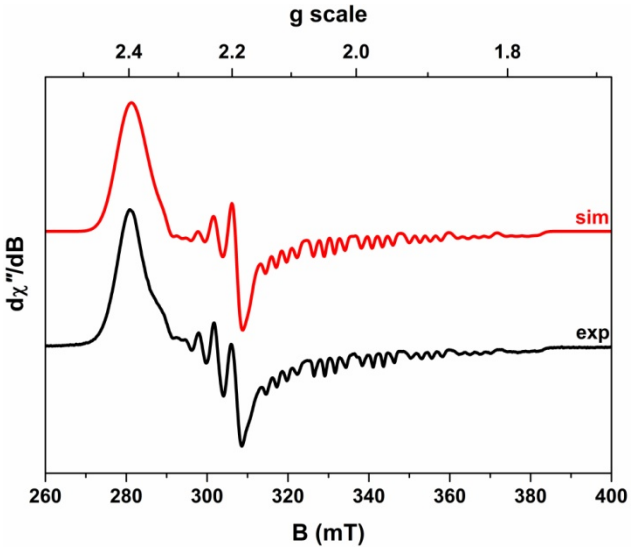

X-band EPR spectrum of recorded in CH_2Cl_2/toluene at 30 K (experimental conditions: frequency, 9.3668 GHz; modulation, 0.5 mT; power, 0.63 mW). Experimental spectrum shown in black and simulation depicted by the red trace: g = (2.280, 2.280, 2.002); $A\{^{59}\text{Co}\}$ = (35, 36, 111) × 10^{-4} cm^{-1}; $A\{^{35,37}\text{Cl}\}$ = (0, 0, 25) × 10^{-4} cm^{-1}.

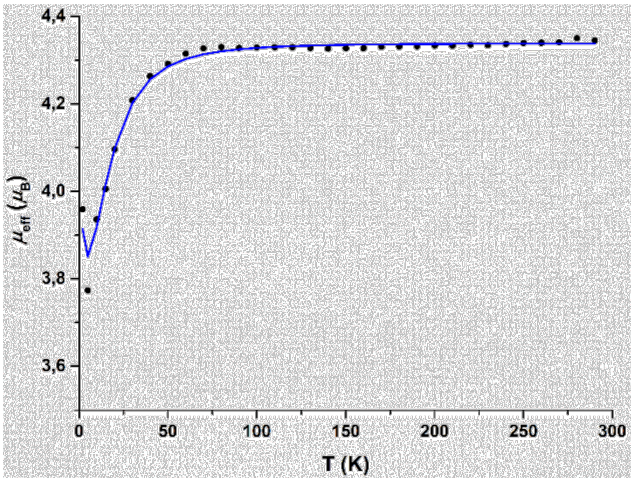

Temperature dependence of the magnetic moment μ_{eff}, μ_B, of a powdered sample of . Filled circles are experimental data; blue line represents the best fit: $S_1 = {}^3/_2$; $S_2 = {}^1/_2$; $g_1 = 2.05$; $g_2 = 2.0$; $J_{12} = 0.47$ cm^{-1}; $|D_2| = 20.37$ cm^{-1}; TIP = 1500×10^{-6} cm^3 mol^{-1}.

DFT-derived (B3LYP) spin density plot for (BS(1,1) calculation on the geometry optimized structure) based on Löwdin population analysis.

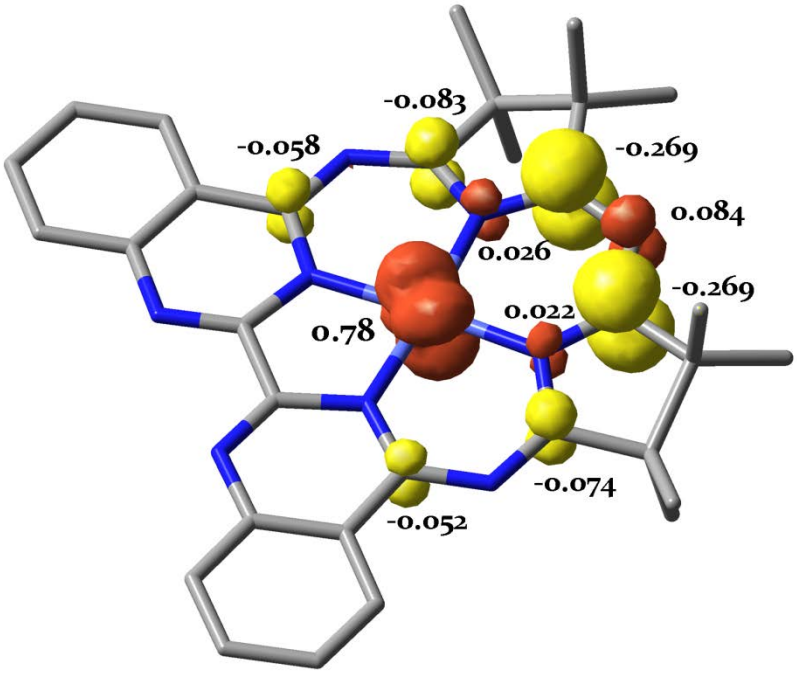

DFT-derived (B3LYP) qualitative MO diagram of (BS(1,1) calculation on the geometry optimized structure).

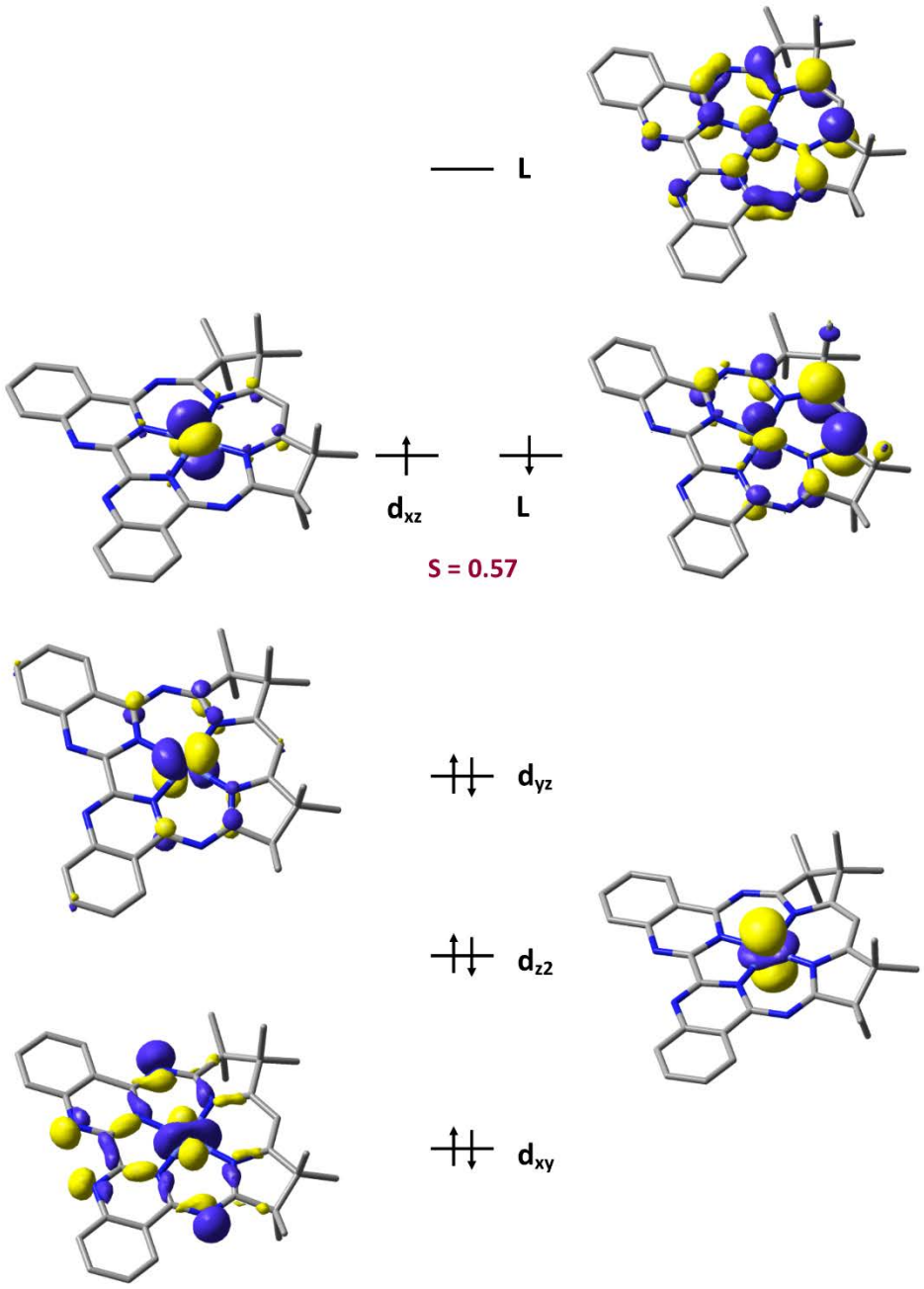

Reduction Potentials (V vs. $Fc^{+/0}$) of – (Oxidation state represents formal metal valency).

$E_{1/2}$ ($Co^{III/II}$)	$E_{1/2}$ ($Co^{II/I}$)	$E_{1/2}$ ($Co^{I/0}$)
0.14	-0.86	E_a: -1.53, E_c: -1.33
0.11	-0.88	E_a: -1.51, E_c: -1.22
0.12	-0.85	–
-0.22	-1.27	-1.78

Crystallographic Data

	$\cdot CH_2Cl_2$	$\cdot 2CH_2Cl_2$	
Empirical formula	$C_{34}H_{35}N_8Cl_4Co$	$C_{35}H_{37}N_8Cl_5Co$	$C_{33}H_{33}N_8Co$
Formula weight	756.43	805.91	600.60
Crystal system	triclinic	monoclinic	orthorhombic
Space group	*P*-1	$P2_1/c$	*Pbca*
a (Å)	10.0493(7)	11.6266(8)	10.199(3)
b (Å)	18.586(1)	21.949(2)	20.351(6)
c (Å)	19.448(1)	15.014(1)	26.781(8)
± (°)	101.466(2)	90.00	90.00
² (°)	104.309(2)	108.541(2)	90.00
³ (°)	103.074(2)	90.00	90.00
Volume ($Å^3$)	3301.4(4)	3632.4(4)	5559(3)
Z	4	4	8
$Á_{calc}$ (mg mm^{-3})	1.522	1.474	1.435
μ (mm^{-1})	0.883	0.879	0.608
F(000)	1560.0	1660.0	2512.0
Reflections collected	55117	50205	36358
Independent refl./R_{int}	18354/0.0331	9196/0.0519	4231/0.0984
Data/restraints/parameters	18354/6/866	9196/0/590	4231/0/511
Goodness-of-fit on F^2	1.027	1.011	1.054
Final R_1 indexes [I e 2Ã(I)]	0.0393	0.0501	0.0484
Final wR_2 indexes [all data]	0.1024	0.1434	0.1267
” $Á_{min,max}$ (e $Å^{-3}$)	0.81/-0.54	0.85/-1.21	0.35/-0.53

Select Bond Distances (Å) for , and .

Co–N1	1.918(1)	1.918(2)	1.877(3)
Co–N2	1.924(1)	1.911(2)	1.878(3)
Co–N3	1.898(1)	1.892(2)	1.857(3)
Co–N4	1.903(1)	1.891(2)	1.864(3)
N3–C13	1.348(2)	1.356(3)	1.374(5)
C13–C14	1.378(2)	1.376(4)	1.381(6)
C14–C15	1.380(2)	1.386(4)	1.368(5)
N4–C15	1.344(2)	1.344(3)	1.368(5)
Co–Cl	2.2685(5) 2.2557(5)	2.4458(7)	

ASSOCIATED CONTENT

. Crystallographic data files (CIF format), additional electrochemical and spectroscopic data. This material is available free of charge via the Internet at http://pubs.acs.org.

AUTHOR INFORMATION

*E-mail: corinna.hess@ch.tum.de

¶Surface Engineering & Tribology Group, CSIR-Central Mechanical Engineering Research Institute, Mahatma Gandhi Avenue, Durgapur 713209, India.

The authors declare no competing financial interests.

ACKNOWLEDGMENT

We are grateful to Andreas Göbels (MPI) for technical assistance with SQUID measurements and to Andy Beeby (Durham) for the use of his instrument for diffuse reflectance spectra. We thank the Diamond Light Source for an award of instrument time on the Station I19 (MT 6749) and the instrument scientists for support. MK thanks the TUM Graduate School for financial support. EP was funded by an EPSRC studentship.

REFERENCES

(1) Dempsey, J. L.; Brunschwig, B. S.; Winkler, J. R.; Gray, H. B. *Acc. Chem. Res.* , *42*, 1995-2004.

(2) Artero, V.; Fontecave, M. *Coord. Chem. Rev.* , *249*, 1518-1535.

(3) Mahammed, A.; Mondal, B.; Rana, A.; Dey, A.; Gross, Z. *Chem. Commun.* , *50*, 2725-2727.

(4) Lei, H.; Han, A.; Li, F.; Zhang, M.; Han, Y.; Du, P.; Lai, W.; Cao, R. *Phys. Chem. Chem. Phys.* , *16*, 1883-1893.

(5) Lee, C. H.; Dogutan, D. K.; Nocera, D. G. *J. Am. Chem. Soc.* , *133*, 8775-8777.

(6) Jacques, P.-A.; Artero, V.; Pe´caut, J.; Fontecave, M. *Proc. Natl. Acad. Sci. U.S.A.* , *106*, 20627-20632.

(7) Hu, X.; Brunschwig, B. S.; Peters, J. C. *J. Am. Chem. Soc.* , *129*, 8988-8998.

(8) Du, P.; Schneider, J.; Luo, G.; Brennessel, W. W.; Eisenberg, R. *Inorg. Chem.* , *48*, 4952-4962.

(9) Dempsey, J. L.; Winkler, J. R.; Gray, H. B. *J. Am. Chem. Soc.* , *132*, 16774-16776.

(10) Fihri, A.; Artero, V.; Razavet, M.; Baffert, C.; Leibl, W.; Fontecave, M. *Angew. Chem. Int. Ed.* , *47*, 564-567.

(11) Artero, V.; Chavarot-Kerlidou, M.; Fontecave, M. *Angew. Chem. Int. Ed.* , *50*, 7238-7266.

(12) Artero, V.; Fontecave, M. *Chem. Soc. Rev.* , *42*, 2338-2356.

(13) Teets, T. S.; Nocera, D. G. *Chem. Commun.* , *47*, 9268-9274.

(14) Dempsey, J. L.; Winkler, J. R.; Gray, H. B. *J. Am. Chem. Soc.* , *132*, 1060-1065.

(15) Bhattacharjee, A.; Chavarot-Kerlidou, M.; Andreiadis, E. S.; Fontecave, M.; Field, M. J.; Artero, V. *Inorg. Chem.* , *51*, 7087-7093.

(16) Roubelakis, M. M.; Bediako, D. K.; Dogutan, D. K.; Nocera, D. G. *Energy Environ. Sci.* , *5*, 7737-7740.

(17) Solis, B. H.; Hammes-Schiffer, S. *Inorg. Chem.* , *53*, 6427-6443.

(18) Kellett, R. M.; Spiro, T. G. *Inorg. Chem.* , *24*, 2373-2377.

(19) Palmer, J. H.; Mahammed, A.; Lancaster, K. M.; Gross, Z.; Gray, H. B. *Inorg. Chem* , *48*, 9309-9315.

(20) Solis, B. H.; Maher, A. G.; Honda, T.; Powers, D. C.; Nocera, D. G.; Hammes-Schiffer, S. *ACS Catal.* , *4*, 4516-4526.

(21) Muresan, N.; Lu, C. C.; Ghosh, M.; Peters, J. C.; M., A.; Henling, L. M.; Weyhermüller, T.; Bill, E.; Wieghardt, K. *Inorg. Chem.* , *47*, 4579-4590.

(22) Lu, C. C.; E. Bill; Weyhermuller, T.; Bothe, E.; Wieghardt, K. *J. Am. Chem. Soc.* , *130*, 3181-3197.

(23) Hess, C. R.; Weyhermüller, T.; Bill, E.; Wieghardt, T. *Inorg. Chem.* , *49*, 5686-5700.

(24) Dzik, W. I.; Xu, X.; Zhang, X. P.; Reek, J. N. H.; De Bruin, B. *J. Am. Chem. Soc.* , *132*, 10891-10902.

(25) Intrieri, D.; Caselli, A.; Gallo, E. *Eur. J. Inorg. Chem.* , 5071-5081.

(26) Cui, X.; Xu, X.; Jin, L.-M.; Wojtas, L.; Zhang, X. P. *Chem. Sci.* , *6*, 1219-1224.

(27) Jin, L.-M.; Lu, H.; Cui, Y.; Lizardi, C.; Arzua, T. N.; Wojtas, L.; Cui, X.; Zhang, X. P. *Chem. Sci.* , *5*, 2422-2427.

(28) Goswami, M.; Lyaskovskyy, V.; Domingos, S. R.; Buma, W. J.; Woutersen, S.; Troeppner, O.; Ivanovi•-Burmazovi•, I.; Lu, H.; Cui, X.; Zhang, X. P.; Reijerse, E. J.; DeBeer, S.; van Schooneveld, M. M.; Pfaff, F. F.; Ray, K.; De Bruin, B. *J. Am. Chem. Soc.* .

(29) Lyaskovskyy, V.; Suarez, A. I. O.; Lu, H.; Jiang, H.; Zhang, X. P.; de Bruin, B. *J. Am. Chem. Soc.* , *133*, 12264-12273.

(30) Müller, E.; Bernardinelli, G.; von Zelewsky, A. *Inorg. Chem.* , *27*, 4645-4651.

(31) Banerjee, P.; Company, A.; Weyhermüller, T.; Bill, E.; Hess, C. R. *Inorg. Chem.* , *48*, 2944-2955.

(32) Hanson, G. R.; Gates, K. E.; Noble, C. J.; Griffin, M.; Mitchell, A.; Benson, S. *J. Inorg. Biochem.* , *98*, 903-916.

(33) Dolomanov, O. V.; Bourhis, L. J.; Gildea, R. J.; Howard, J. A. K.; Puschmann, H. *J. Appl. Cryst.* , *42*, 339-341.

(34) Sheldrick, G. M. *Acta Cryst.* , *A64*, 112-122.

(35) Neese, F. In *ORCA - an ab initio, DFT and semiempirical SCF-MO package, version 2.9.1* Max Planck Insitut für Bioanorganische Chemie, Mülheim an der Ruhr, 2009.

(36) Becke, A. D. *J. Chem. Phys* , *84*, 4524-4529.

(37) Becke, A. D. *J. Chem. Phys* , *98*, 5648-5652.

(38) Lee, C. T.; Yang, W. T.; Parr, R. G. *Phys. Rev. B* , *37*, 785-789.

(39) Ahlrichs, R.; May, K. *Phys. Chem. Chem. Phys.* , *2*, 943-945.

(40) Weigend, F.; Ahlrichs, R. *Phys. Chem. Chem. Phys.* , *7*, 3297-3305.

(41) Schäfer, A.; Huber, C.; Ahlrichs, R. *J. Chem. Phys* , *100*, 5829-5835.

(42) Schäfer, A.; Horn, H.; Ahlrichs, R. *J. Chem. Phys* , *97*, 2571-2577.

(43) Eichkorn, K.; Treutler, O.; Öhm, H.; Häser, M.; Ahlrichs, R. *Chem. Phys. Lett.* , *242*, 652-660.

(44) Eichkorn, K.; Weigend, F.; Treutler, O.; Ahlrichs, R. *Chem. Phys. Lett.* , *240*, 283-290.

(45) Ginsberg, A. P. *J. Am. Chem. Soc.* , *102*, 111-117.

(46) Noodleman, L.; Peng, C. Y.; Case, D. A.; Mouesca, J. M. *Coord. Chem. Rev.* , *144*, 199-244.

(47) Kirchner, B.; Wennmohs, F.; Ye, S.; Neese, F. *Curr. Opin. Chem. Biol.* , *11*, 134-141.

(48) Neese, F. *J. Phys. Chem. Solids* , *65*, 781-785.

(49) *GaussView 4.1.2; Gaussian, Inc.:* Wallington, CT, 2006.

(50) Liptak, M. D.; Brunold, T. C. *J. Am. Chem. Soc.* , *128*, 9144-9156.

(51) Bhattarcharjee, A.; Chavarot-Kerlidou, M.; Dempsey, J. L.; Gray, H. B.; Fujita, E.; Muckerman, J. T.; Fontecave, M.; Artero, V.; Arantes, G. M.; Field, M. J. *ChemPhysChem* , *15*, 2951-2958.

(52) The peak to peak separation for all three redox processes in the CV of 4 is 125 - 150 mV, however, the peak to peak separation for the Fc+/0 couple was also determined to be 134 mV in THF. Values for ia/ic = 0.9 - 1.

(53) Gavrilova, A. L.; Bosnich, B. *Inorg. Chim. Acta* , *352*, 24-30.

(54) La Mar, G. N.; Walker, F. A. *J. Am. Chem. Soc.* , *95*, 1790-1796.
(55) McGarvey, B. M. *Can. J. Chem.* , *53*, 2498-2511.
(56) Assour, J. M. *J. Am. Chem. Soc.* , *87*, 4701-4706.
(57) Baumgarten, M.; Winscom, C. J.; Lubitz, W. *Appl. Magn. Reson.* , *20*, 35-70.
(58) Cariati, F.; Galizzioli, D.; Morazzoni, F.; Busetto, C. *J. Chem. Soc., Dalton Trans.* , 556-561.
(59) Ozarowski, A.; Lee, H. M.; Balch, A. L. *J. Am. Chem. Soc.* , *125*, 12606-12614.
(60) Walker, F. A. *J. Am. Chem. Soc.* , *92*, 4235-4244.
(61) Walker, F. A. *J. Magn. Reson.* , *15*, 201-218.
(62) Wayland, B. B.; Abd-Elmageed, M. E. *J. Am. Chem. Soc.* , *96*, 4809-4814.
(63) Hamilton, J. A.; Yamada, R.; Blakley, R. L.; Hogenkamp, H. P. C.; Looney, F. D.; Winfield, M. E. *Biochemistry* , *10*, 347-355.
(64) Jörin, E.; Schweiger, A.; Günthard, H. H. *J. Am. Chem. Soc.* , *105*, 4277-4286.
(65) Adamian, V. A.; D'Souza, F.; Licoccia, S.; Di Vona, M. L.; Tassoni, E.; Paolesse, R.; Boschi, T.; Kadish, K. M. *Inorg. Chem.* , *34*, 532-540.
(66) Hush, N. S.; Woolsey, I. S. *J. Chem. Soc., Dalton Trans.* , 24-34.
(67) Murakami, Y.; Matsuda, Y.; Sakata, K.; Yamada, S.; Tanaka, Y.; Aoyama, Y. *Bull. Chem. Soc. Jpn.* , *54*, 163-169.
(68) Ramdhanie, B.; Telser, J.; Caneschi, A.; Zakharov, L. N.; Rheingold, A. L.; Goldberg, D. P. *J. Am. Chem. Soc.* , *126*, 2515-2525.
(69) Pezeshk, A. *Inorg. Chem.* , *31*, 2282-2284.
(70) Pzeshk, A.; Greenway, F. T.; Dabrowiak, J. C.; Vincow, G. *Inorg. Chem.* , *17*, 1717-1725.
(71) Abusamleh, A. S.; Chmielewski, P. J.; Warburton, P. R.; Morales, L.; Stephenson, N. A.; Busch, D. A. *J. Coord. Chem.* , *23*, 91-111.
(72) Endicott, J. F.; Lilie, J.; Kuszaj, J. M.; Ramaswamy, B. S.; Schmonsees, W. G.; Simic, M. G.; Glick, M. D.; Rillema, D. P. *J. Am. Chem. Soc.* , *99*, 429-439.
(73) Bo•a, R.; Miklovi•, J.; Titia, J. *Inorg. Chem.* , *53*, 2367-2369.
(74) Ideaicová, M.; Titia, J.; Krzystek, J.; Bo•a, R. *Inorg. Chem.* , *52*, 9409-9417.
(75) Saber, M. R.; Dunbar, K. R. *Chem. Commun.* , *50*, 12266-12269.
(76) Titia, J.; Miklovi•, J.; Bo•a, R. *Inorg. Chem. Commun.* , *35*, 72-75.
(77) Yang, F.; Zhou, Q.; Zhang, Y.; Zeng, G.; Li, G.; Shi, Z.; Wang, B.; Feng, S. *Chem. Commun.* , *49*, 5289-5291.
(78) Rosa, V.; Gonzalez, P. J.; Avilés, T.; Gomes, P. T.; Welter, R.; Rizzi, A. C.; Passeggi, M. C. G.; Brondino, C. D. *Eur. J. Inorg. Chem.* , 4761-4769.
(79) Sproules, S.; Kapre, R. R.; Roy, N.; Weyhermüller, T.; Wieghardt, K. *Inorg. Chim. Acta* , *363*, 2702-2714.

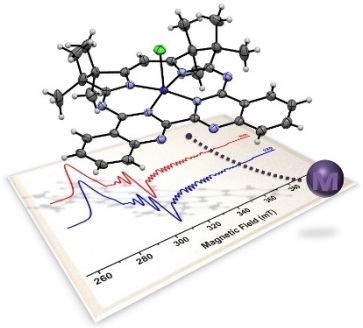

The synthesis and characterization of a series of cobalt complexes, coordinated by a redox-active macrocyclic biquinazoline ligand (Mabiq) are described. A dicobaltous form provides the first example of a bimetallic Mabiq-complex. The redox series of monometallic compounds includes the square-planar Co^{I} species, one of a few examples of structurally characterized low-valent N_4-macrocyclic compounds.

Supplementary Information

A series of [Co(Mabiq)Cl_{2-n}] (n = 0, 1, 2) compounds and evidence for the elusive bimetallic form.

Emma V. Puttock,[‡] *Priyabrata Banerjee,*[§,¶] *Manuel Kaspar,*[†] *Liam Drennen,*[‡] *Dmitry S. Yufit,*[‡] *Eckhard Bill,*[§] *Stephen Sproules,*[‖] *Corinna R. Hess**[,†]

[†]Department of Chemistry and Catalysis Research Center, Technische Universität München, Lichtenbergstrasse 4, D-85747 Garching, Germany

[‡]Department of Chemistry, Durham University, South Rd, Durham, DH1 3LE, United Kingdom

[§]Max-Planck-Institut für Chemische Energiekonversion, Stiftstrasse 34-36, D-45470 Mülheim an der Ruhr, Germany

[‖]WestCHEM, School of Chemistry, University of Glasgow, Glasgow, G12 8QQ, United Kingdom

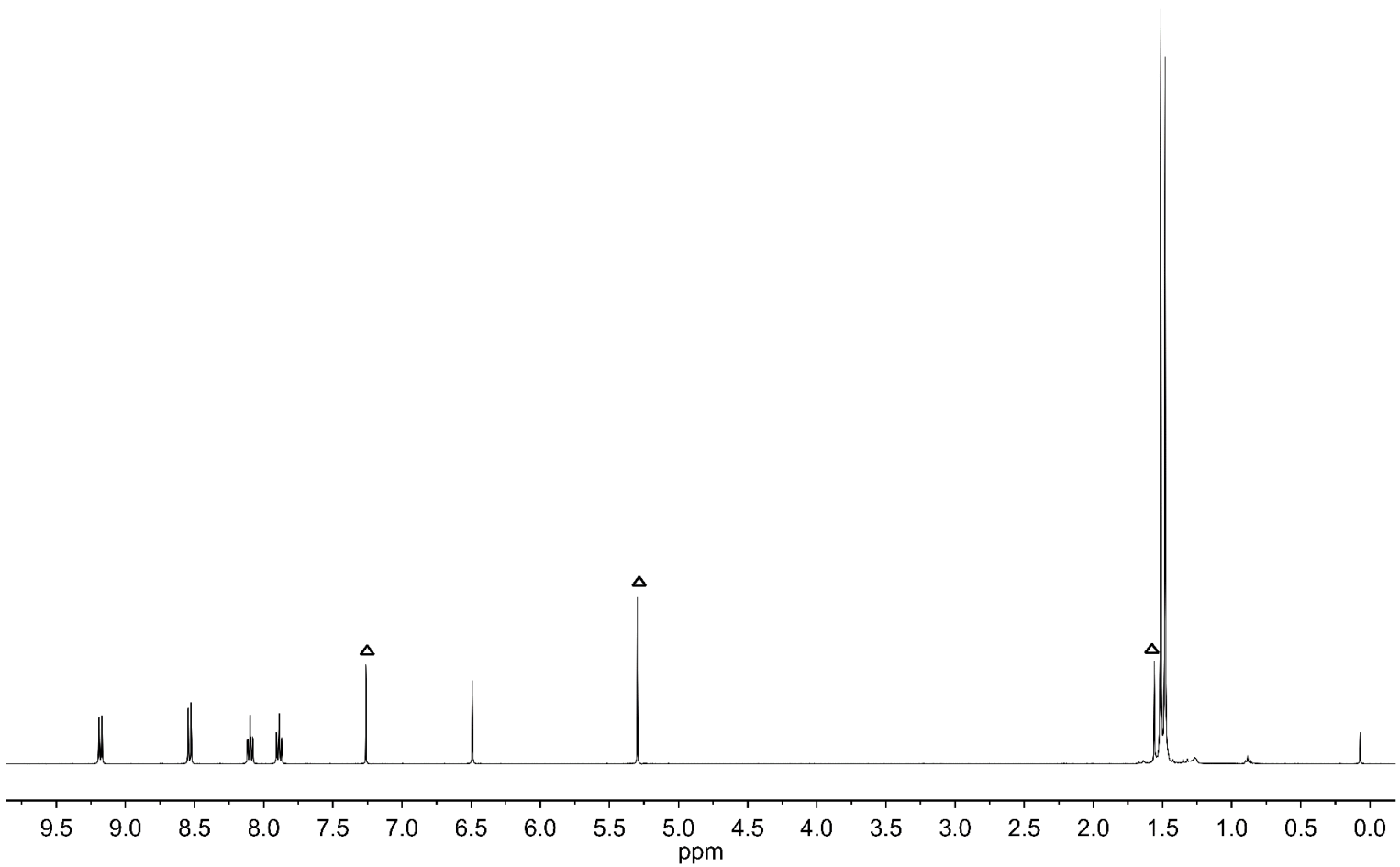

Figure S1. ^{1}NMR (400 MHz, $CDCl_3$) of **1**; △ = solvent peaks ($CDCl_3$ solvent residual signal, CH_2Cl_2 and H_2O).

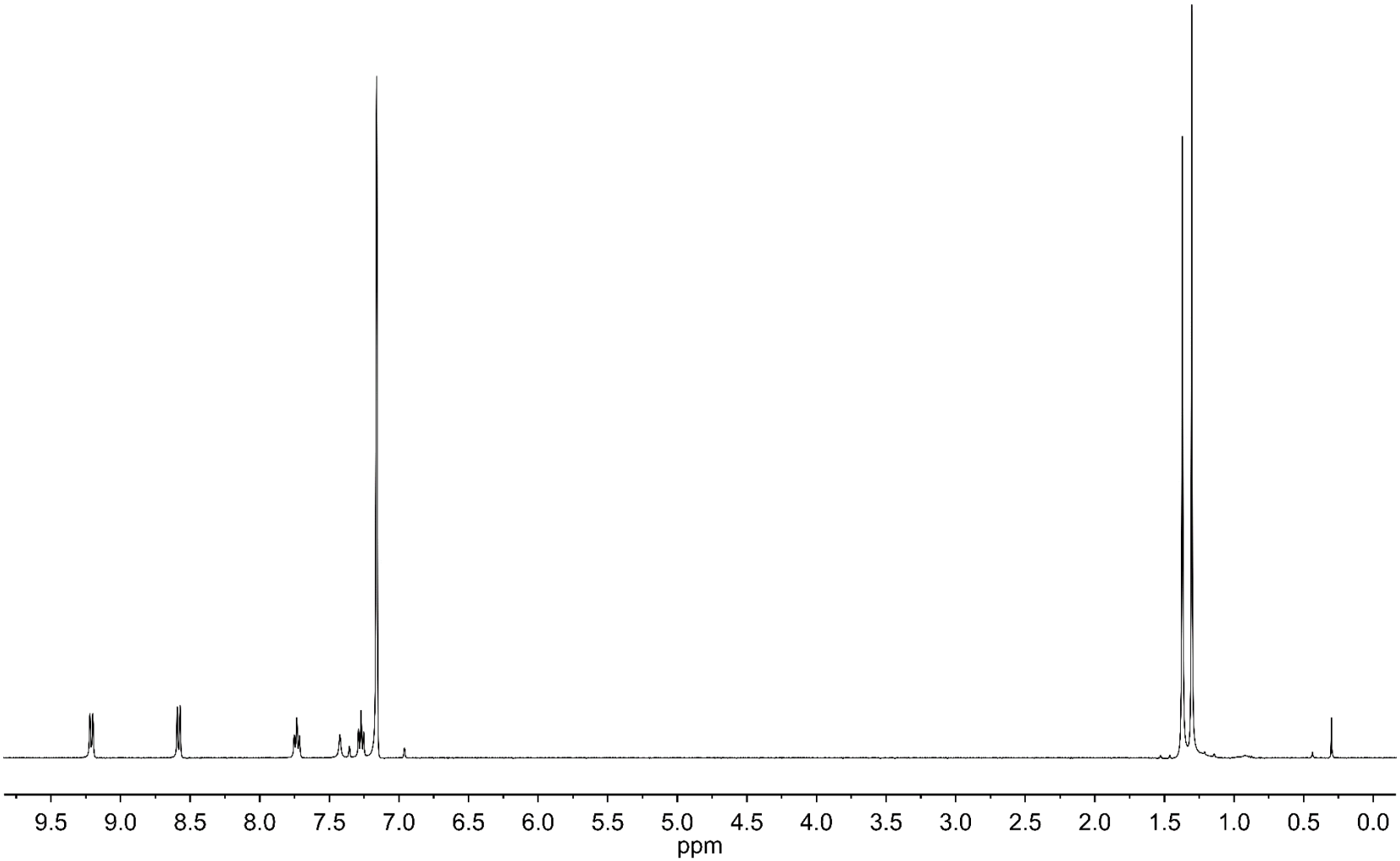

Figure S2. ^{1}H NMR (400 MHz, C_6D_6) of **4**: δ = 9.21 (d, *J* = 8.1 Hz, 2H), 8.58 (d, *J* = 8.2 Hz, 2H), 7.73 (t, *J* = 7.5, 2H), 7.42 (s, 1H), 7.27 (t, *J* = 7.6, 2H), 1.37 (s, 12H), 1.30 (s, 12H).

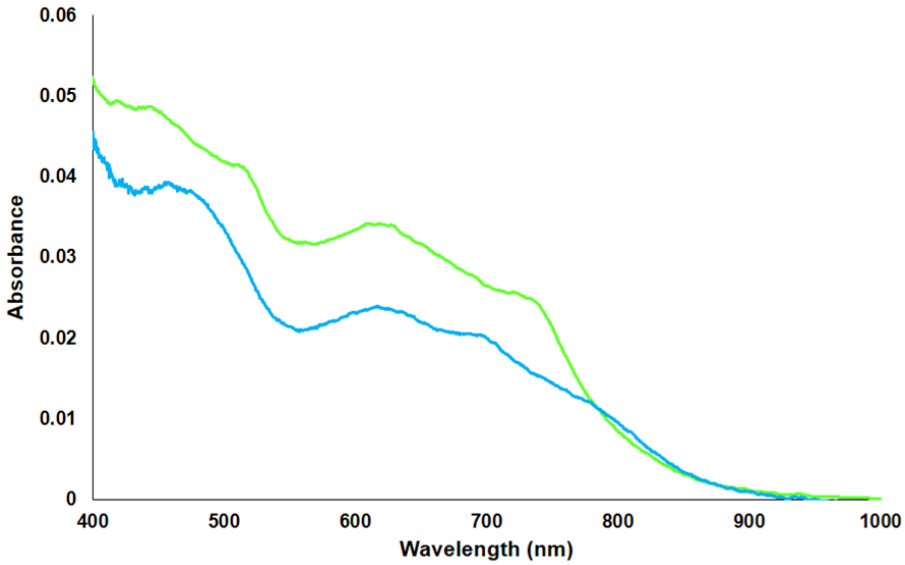

Figure S3. Solid state electronic spectra of **2** (green) and **3** (blue).

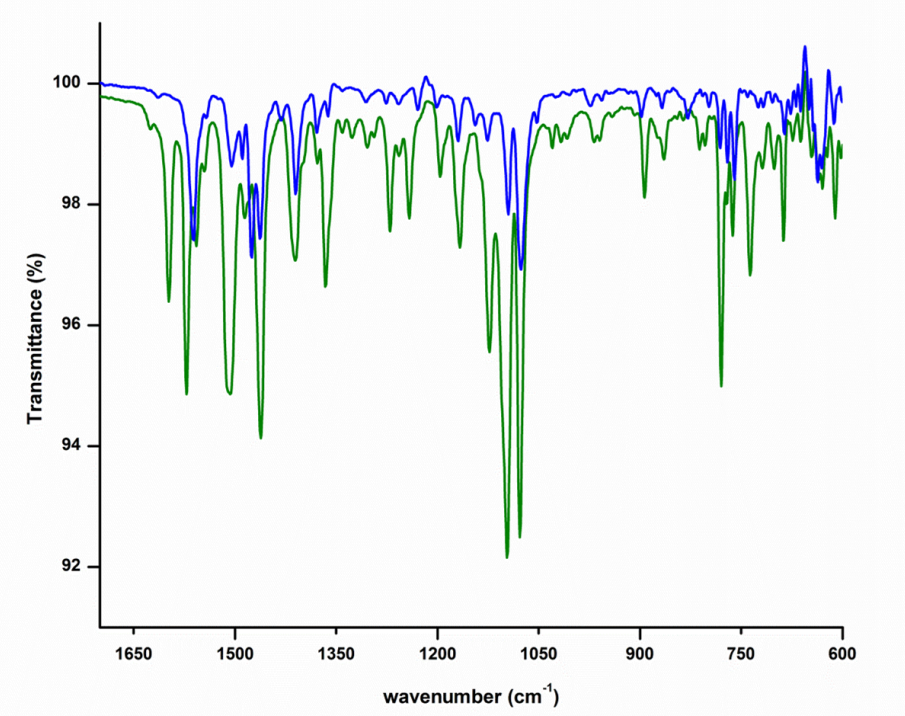

Figure S4. Comparison of IR spectra of **2** (green) and **3** (blue).

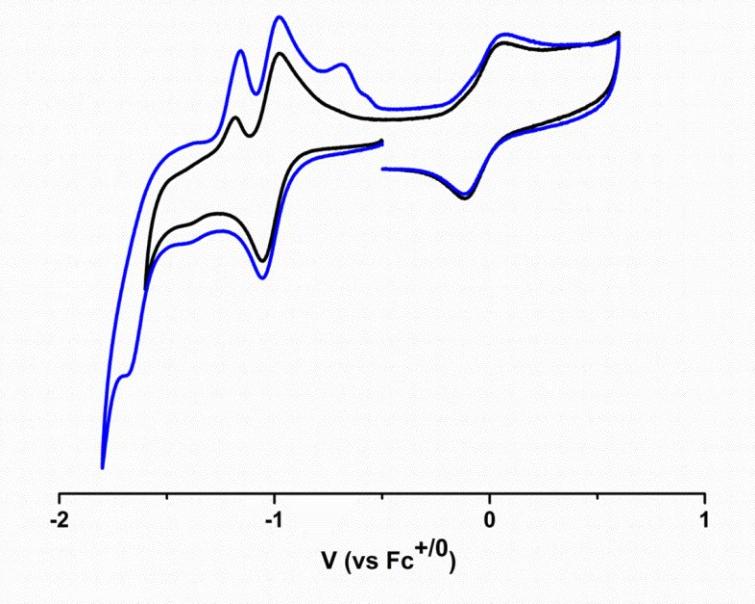

Figure S5. Cyclic voltammogram of **3**, MeOH, showing effect of scanning at potentials < -1.2 V; 0.2 V s^{-1}, 0.1 M $[N(n\text{-}Bu)_4]PF_6$.

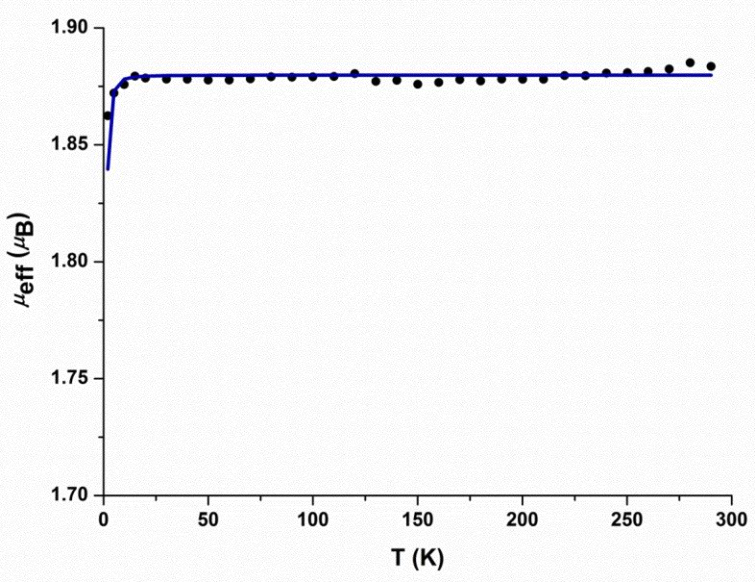

Figure S6. Temperature dependence of the magnetic moment μ_{eff}, μ_B, (2 – 300 K, 1T) of a crystalline sample of **2**. Filled circles are experimental data; blue line represents the best fit: S_1 = $^1/_2$; $g_1 = 2.17$; TIP = 61×10^{-6} cm^3 mol^{-1}.

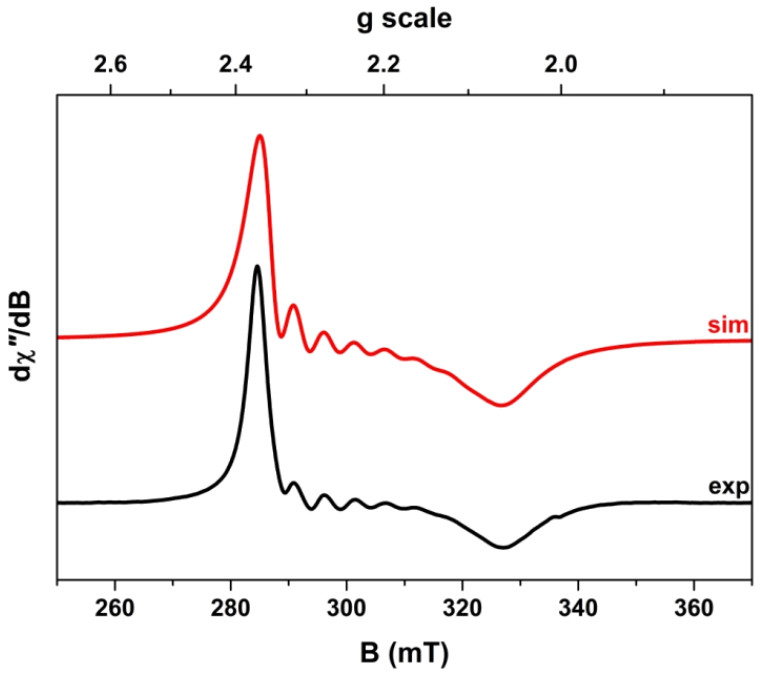

Figure S7. X-band EPR spectrum of **2** recorded in CH_2Cl_2/toluene at 293 K (experimental conditions: frequency, 9.4338 GHz; modulation, 0.7 mT; power, 20 mW). Experimental spectrum shown in black and simulation depicted by the red trace: g_{iso} = 2.204; A_{iso} = 55 × 10^{-4} cm^{-1}.

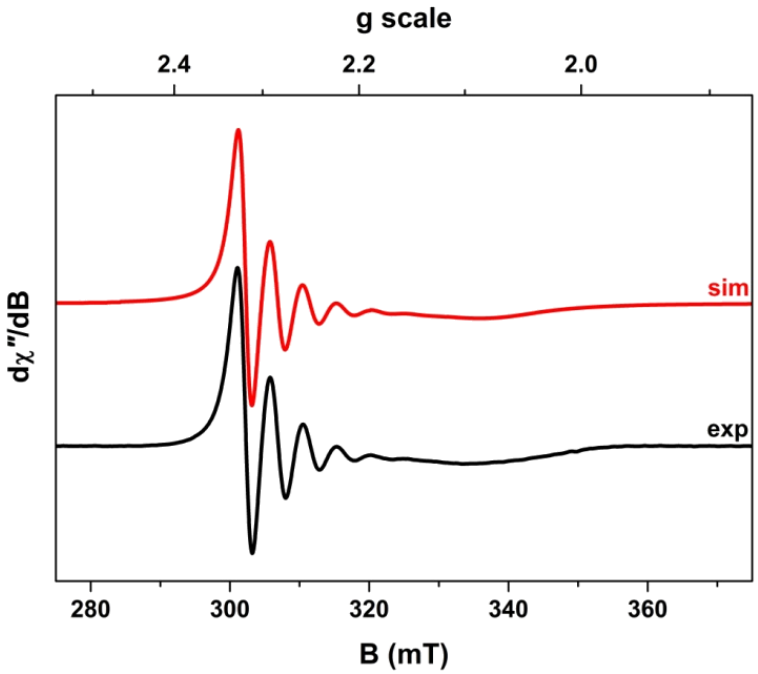

Figure S8. X-band EPR spectrum of **3** recorded in CH_3OH at 293 K (experimental conditions: frequency, 9.8079 GHz; modulation, 0.4 mT; power, 20 mW). Experimental spectrum shown in black and simulation depicted by the red trace: $g_{iso} = 2.196$; $A_{iso} = 49 \times 10^{-4}$ cm^{-1}.

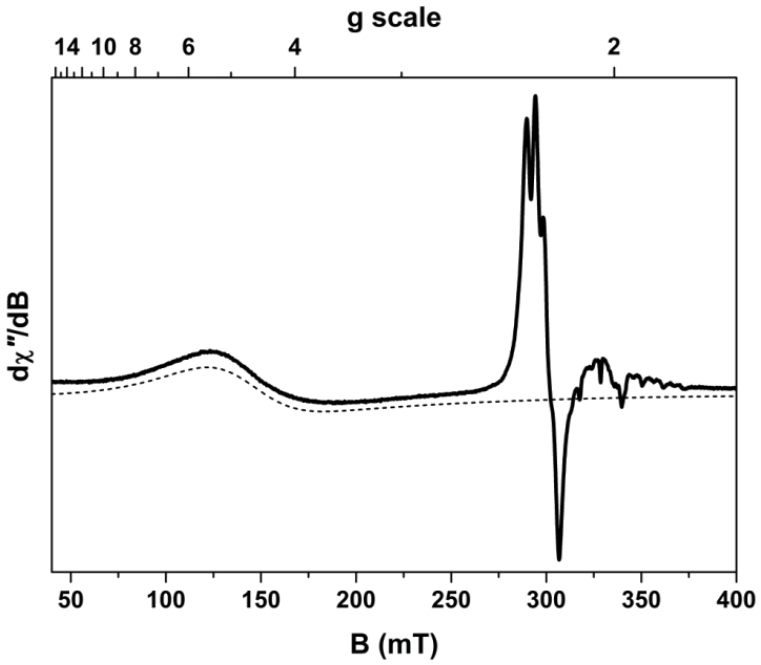

Figure S9. X-band EPR spectra of **3** recorded in CH_3OH/toluene at 10 K (experimental conditions: frequency, 9.3352 GHz; modulation, 0.6 mT; power, 0.63 mW). Experimental data are depicted by the solid line. Simulation of an $S = {}^3/_2$ spectrum of a tetrahedral Co^{II} center with $D >> h\nu$ is shown by the dashed line: $g = (2.35, 2.35, 2.58)$; $E/D = 0.03$; $W = (450, 450, 1000) \times 10^{-4}$ cm^{-1}; $\sigma_{E/D} = 0.22$.

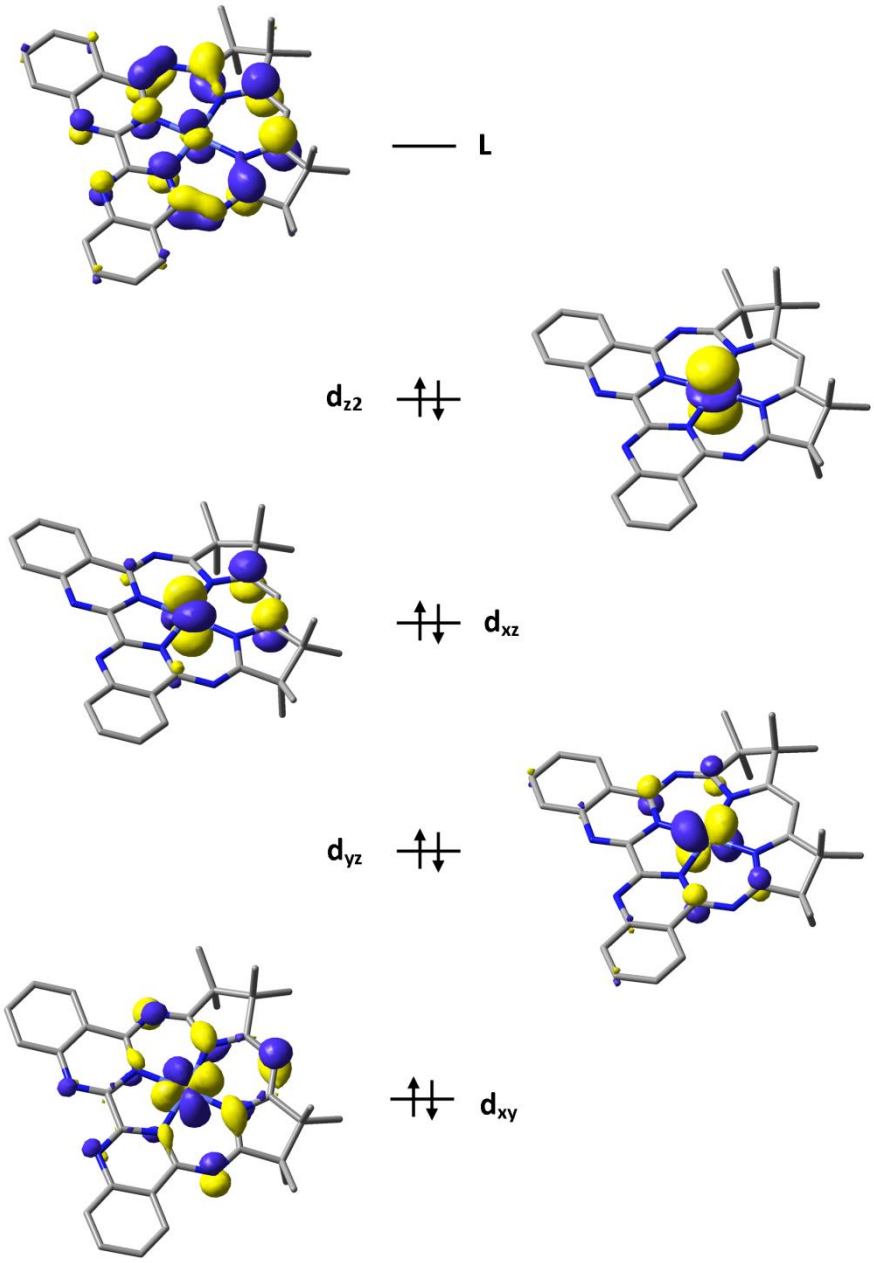

Figure S10. DFT-derived (B3LYP) qualitative MO diagram of **4** (UKS calculation on the geometry optimized structure).

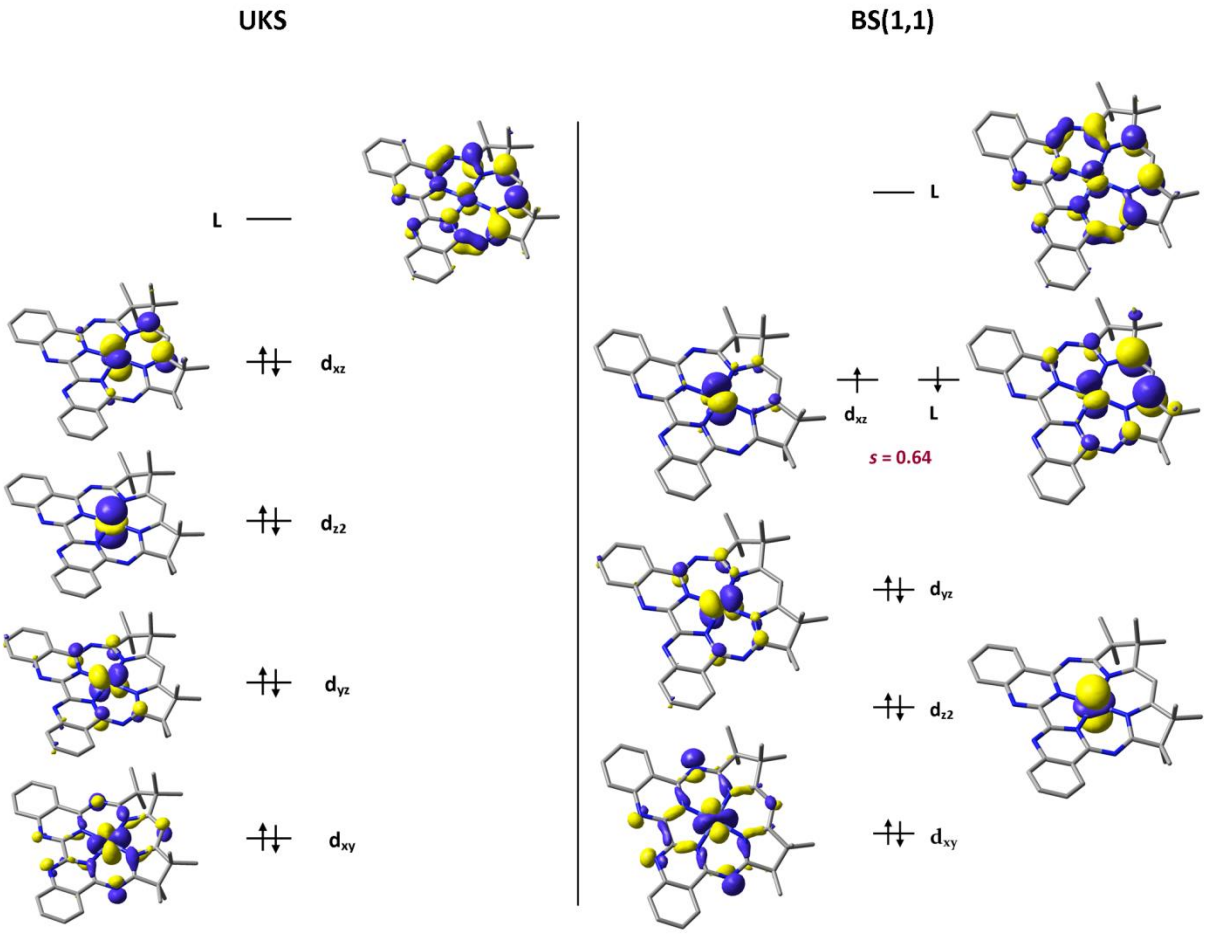

Figure S11. Qualitative MO diagrams from DFT calculations (B3LYP) on the unoptimized, crystallographically determined structure of **4**. Left: results from UKS calculation, right: results from BS(1,1) calculation.

Table S1. Selected Bond Distances (Å) and Angles (°) in the DFT optimized structure of **4**.

	UKS	**BS(1,1)**
Co–N1	1.912	1.919
Co–N2	1.912	1.917
Co–N3	1.898	1.909
Co–N4	1.898	1.908
N3–C13	1.357	1.375
C13–C14	1.391	1.389
C14–C15	1.391	1.386
N4–C15	1.357	1.376
ψ(N6–C10–C11–N7)[a]	-0.04	-0.11

[a] Crystallographically determined, ψ(N6–C10–C11–N7) = -6.35°

Table S2. DFT Optimized Geometry (.XYZ format) for **4**; ORCA, B3LYP, BS(1,1) calculation.

```
---------------------------------
CARTESIAN COORDINATES (ANGSTROEM)
---------------------------------
  Co    -0.005046    0.059299    0.001590
  N      1.334344    0.049225   -1.370405
  N     -1.242684   -0.080120   -1.458073
  N     -1.437715    0.076892    1.262747
  N      1.329910    0.212350    1.356346
  N      1.510085    0.065183   -3.763977
  N     -1.257716   -0.070644   -3.857934
  N     -3.279722   -0.275865   -0.246310
  N      3.295124    0.048101   -0.024680
  C      0.829221    0.034323   -2.660113
  C     -0.652456   -0.039572   -2.710473
  C     -2.624843   -0.160238   -3.851645
  C     -3.320007   -0.188294   -5.085212
  C     -4.700898   -0.286429   -5.097831
  C     -5.423669   -0.360784   -3.884188
  C     -4.760537   -0.334538   -2.667410
  C     -3.350744   -0.231593   -2.633067
  C     -2.592186   -0.190380   -1.397911
  C     -2.737381   -0.167912    0.939258
  C     -3.588911   -0.375271    2.192416
  C     -2.723094    0.391681    3.258939
  C     -1.341108    0.273281    2.621380
  C     -0.135266    0.428731    3.290934
  C      1.122952    0.393948    2.703461
  C      2.440557    0.646439    3.432285
  C      3.446698   -0.030965    2.430554
  C      2.666254    0.097604    1.121869
  C      2.682365    0.070912   -1.219322
  C      3.522204    0.110209   -2.401139
  C      4.934202    0.149175   -2.340737
  C      5.676731    0.193516   -3.510401
  C      5.033253    0.199048   -4.769829
  C      3.651505    0.158133   -4.849890
  C      2.876309    0.112714   -3.665905
  C     -3.614439   -1.902951    2.454245
  C     -5.031986    0.119137    2.033227
  C     -2.809150   -0.177715    4.683621
  C     -3.086753    1.898733    3.311222
  C      2.486244    0.086772    4.862566
  C      2.651011    2.181768    3.499429
  C      3.599768   -1.549873    2.699724
  C      4.843338    0.599514    2.368670
  H     -2.733819   -0.131419   -6.005516
  H     -5.238779   -0.308122   -6.050759
  H     -6.514879   -0.440140   -3.908104
  H     -5.304279   -0.391494   -1.723333
  H     -0.179669    0.598802    4.368105
```

H	5.416558	0.144559	-1.362273
H	6.769528	0.224425	-3.460704
H	5.633284	0.234905	-5.684587
H	3.125485	0.158678	-5.807537
H	-2.601538	-2.312548	2.612122
H	-4.227072	-2.140633	3.341314
H	-4.058235	-2.418184	1.585279
H	-5.085075	1.160551	1.679232
H	-5.573441	0.047936	2.994524
H	-5.564539	-0.503147	1.295777
H	-3.858692	-0.196887	5.029398
H	-2.249168	0.456473	5.393438
H	-2.403192	-1.199277	4.757692
H	-4.087836	2.054087	3.750444
H	-2.354322	2.438515	3.936393
H	-3.074246	2.359397	2.308357
H	1.821976	0.663306	5.530642
H	2.177180	-0.969435	4.915228
H	3.507680	0.168805	5.276653
H	2.661164	2.638821	2.494771
H	3.600645	2.434182	4.003252
H	1.829336	2.647593	4.070889
H	2.621964	-2.053792	2.792101
H	4.171945	-1.730727	3.626344
H	4.147264	-2.018697	1.864305
H	5.482853	0.031578	1.673464
H	4.821403	1.641437	2.013013
H	5.320661	0.579878	3.365694

Table S3. DFT Optimized Geometry (.XYZ format) for **4**; ORCA, B3LYP, UKS calculation.

```
---------------------------------
CARTESIAN COORDINATES (ANGSTROEM)
---------------------------------
  Co    -0.004800    0.044791   -0.001011
  N      1.329232    0.026825   -1.371204
  N     -1.234835   -0.100961   -1.457620
  N     -1.423151    0.078028    1.260473
  N      1.314709    0.213577    1.352250
  N      1.513522    0.042406   -3.767004
  N     -1.257834   -0.095384   -3.860645
  N     -3.272101   -0.275064   -0.241075
  N      3.286929    0.047992   -0.019524
  C      0.829938    0.007839   -2.662756
  C     -0.650082   -0.066143   -2.712718
  C     -2.622865   -0.172425   -3.852771
  C     -3.322312   -0.198923   -5.085224
  C     -4.702990   -0.282784   -5.093038
  C     -5.422919   -0.344257   -3.875168
  C     -4.757937   -0.319501   -2.660744
  C     -3.345273   -0.230731   -2.629671
  C     -2.579472   -0.194061   -1.404607
  C     -2.739614   -0.167148    0.936092
  C     -3.586696   -0.373451    2.190743
  C     -2.715103    0.391494    3.252821
  C     -1.338186    0.287119    2.598218
  C     -0.135644    0.455644    3.276740
  C      1.120221    0.409547    2.680527
  C      2.433625    0.647390    3.424686
  C      3.443215   -0.031201    2.428403
  C      2.667732    0.097960    1.118409
  C      2.669824    0.066771   -1.227338
  C      3.516318    0.112435   -2.397781
  C      4.929602    0.166518   -2.333172
  C      5.673911    0.213854   -3.499930
  C      5.035109    0.207413   -4.763733
  C      3.655640    0.151573   -4.849411
  C      2.875705    0.102796   -3.667015
  C     -3.617404   -1.900700    2.455791
  C     -5.029060    0.124773    2.035610
  C     -2.780932   -0.187077    4.675301
  C     -3.081907    1.896879    3.318699
  C      2.460316    0.079453    4.852562
  C      2.649689    2.181083    3.502389
  C      3.596700   -1.549407    2.702471
  C      4.840267    0.598985    2.369933
  H     -2.737913   -0.152000   -6.007266
  H     -5.244874   -0.303354   -6.043708
  H     -6.515002   -0.412866   -3.896256
  H     -5.300825   -0.367420   -1.715756
```

H	-0.180754	0.634742	4.351486
H	5.409689	0.170187	-1.353668
H	6.766258	0.256060	-3.447132
H	5.639313	0.245823	-5.675621
H	3.132960	0.142879	-5.808875
H	-2.605853	-2.316352	2.605395
H	-4.225067	-2.134410	3.347302
H	-4.069632	-2.413865	1.590101
H	-5.080533	1.166894	1.683577
H	-5.569375	0.052489	2.997500
H	-5.563618	-0.495193	1.297681
H	-3.827929	-0.223063	5.026915
H	-2.225979	0.450789	5.385536
H	-2.361193	-1.203581	4.740815
H	-4.076413	2.043052	3.775160
H	-2.342760	2.437225	3.935419
H	-3.087412	2.362868	2.318499
H	1.802051	0.662650	5.520528
H	2.135751	-0.972372	4.898034
H	3.480824	0.143506	5.271678
H	2.677787	2.643276	2.500674
H	3.593060	2.422842	4.022466
H	1.822839	2.649577	4.064094
H	2.619932	-2.056220	2.788034
H	4.163400	-1.727182	3.632986
H	4.150277	-2.018024	1.871092
H	5.480468	0.030688	1.675705
H	4.819511	1.640960	2.014503
H	5.315830	0.578437	3.367786

Table S4. Final single point energy (Eh) obtained from DFT calculations on **4**.

B3LYP, BS(1,1), geometry optimized structure	-3096.383866388508
B3LYP, UKS, geometry optimized structure	-3096.379833454749
B3LYP, BS(1,1), experimental structure	-3095.894982808677
B3LYP, UKS, experimental structure	-3095.891316739858